Modeling and understanding turbulent mixing in a macrotidal salt wedge estuary

B. Wang,[1] S. N. Giddings,[1] O. B. Fringer,[1] E. S. Gross,[1] D. A. Fong,[1] and S. G. Monismith[1]

Received 20 January 2010; revised 26 October 2010; accepted 8 December 2010; published 25 February 2011.

[1] A high-resolution three-dimensional numerical simulation is performed with the parallel, unstructured grid SUNTANS model to study the spatiotemporal dynamics of turbulent mixing in a shallow, macrotidal salt wedge estuary that experiences periodic mixing and strong stratification. Unresolved vertical mixing is parameterized with the $k - kl$ closure scheme with the Canuto-A stability functions based on a careful comparison of multiple two-equation closure schemes and stability functions via the generic length scale approach. The predictions of velocity, salinity, Richardson number, and Reynolds stress are in good agreement with field observations, and the top and bottom salinity predictions achieve skill scores of 0.86 and 0.91, respectively. The model shows that the salt wedge starts to strengthen upstream at the beginning of weak ebb and gradually expands downstream during the weak tide. Mixing is most active along a density interface during the weak ebb, while it is most active in a bottom mixed layer during weak flood, consistent with the findings inferred from the observations. Stratification decays during the strong ebb in a mixing event along the horizontal extent of the salt wedge while it is also being advected offshore. Local mixing is shown to account for roughly half of the decay rate of the stratification in this process. Numerical experiments are performed to investigate the response of stratification and mixing to changes in the magnitude of the buoyancy. High sensitivity is shown under intermediate levels of stratification that occur in the real system, which becomes considerably weaker under more extreme conditions.

Citation: Wang, B., S. N. Giddings, O. B. Fringer, E. S. Gross, D. A. Fong, and S. G. Monismith (2011), Modeling and understanding turbulent mixing in a macrotidal salt wedge estuary, *J. Geophys. Res.*, *116*, C02036, doi:10.1029/2010JC006135.

1. Introduction

[2] The interplay between stratification and turbulent mixing in response to barotropic straining and baroclinic circulation is a fundamental characteristic of estuaries. Stratification can change substantially over seasonal [*MacCready*, 1999; *Monismith et al.*, 2002], spring-neap [*Nunes Vaz et al.*, 1989; *Jay and Smith*, 1990b; *Peters*, 1997; *Yanagi et al.*, 2003] and tidal [*Jay and Smith*, 1990a; *Simpson et al.*, 1990; *Nepf and Geyer*, 1996; *Stacey et al.*, 1999a; *Ralston and Stacey*, 2005] time scales. The dynamics is most profound in an estuary with strong tidal forcing and substantial fresh river flow, where vertical mixing and stratification can vary strongly both spatially and temporally. This variability has important implications for ocean-estuary exchange and sediment transport [*Nunes Vaz et al.*, 1989].

[3] The primary focus of this work is to understand the tidal time scale hydrodynamics and turbulent mixing processes in a shallow, macrotidal salt wedge estuary. The tidal straining mechanism [*Simpson et al.*, 1990] plays an important role in causing ebb/flood tidal asymmetries because, in general, the straining of the longitudinal density gradient acts to stabilize the water column during ebbs while it destabilizes the water column during floods. The varying strength and pattern of the tidal forcing is also important. Mixed semidiurnal systems, such as Possession Sound [*Wang et al.*, 2009], often exhibit large diurnal inequality, possibly leading to a wide range of stratification conditions. If the tidal flow is strong enough during the strong tide, the stratification can be significantly impacted by local mixing regardless of the flow direction.

[4] To date, attempts to understand the intratidal variability of stratification and mixing in estuarine systems have mainly been based on analyses of field observations. For instance, *Nepf and Geyer* [1996] found that during the strongly stratified periods in the Hudson River estuary, active mixing occurs in the regions of stratification during the ebb tide and occurs in a uniform bottom layer during the flood. *Stacey et al.* [1999a] examined the turbulence near Grizzly Bay in San Francisco Bay and found that energetic mixing is consistently confined near the bottom beneath the stratified upper layer. *Ralston and Stacey* [2005] studied tidal hydrodynamics in a channel through an intertidal

[1]Environmental Fluid Mechanics Laboratory, Stanford University, Stanford, California, USA.

0148-0227/11/2010JC006135

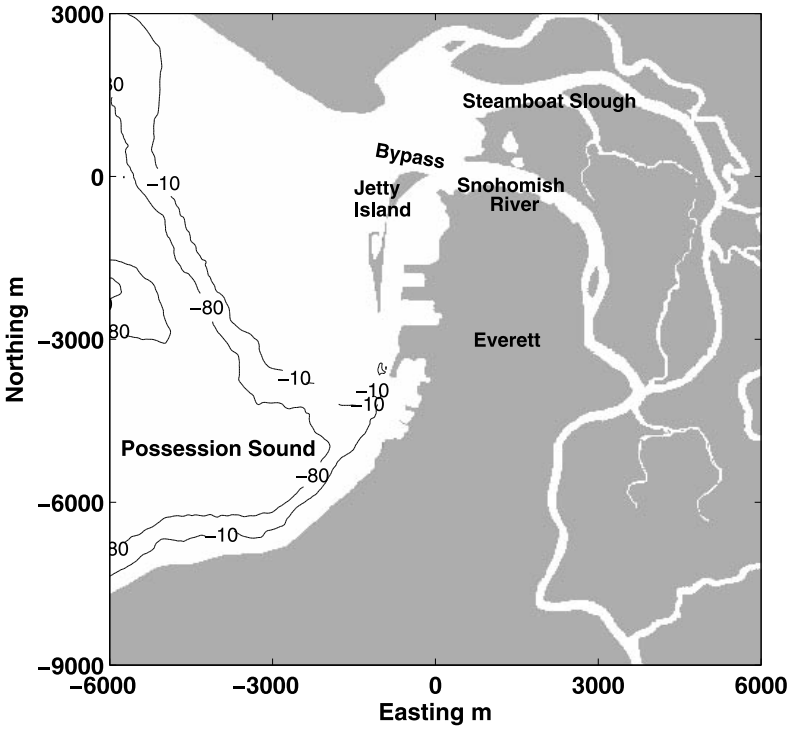

Figure 1. The Snohomish River estuary. Grey zones are highland. Contour lines are for 10 m and 80 m below MML. The horizontal axes are northing and easting of UTM Zone 10 N shifted so that the origin is located close to the north tip of Jetty Island (558,442 m, 5,318,790 m) in UTM coordinates. The northing and easting axes in Figure 2 are relative to this location.

mudflat in San Francisco Bay and reported high variability of turbulent mixing during strong and weak tide periods in this shallow system. While field observations provide much insight into physical processes, they can be limited in spatial and temporal resolution of mixing dynamics.

[5] In the present work, we examine the detailed spatio-temporal features of periodic stratification using a high-resolution three-dimensional hydrodynamic model. The estuary we study is the Snohomish River estuary in Possession Sound near the city of Everett, WA (see Figure 1). It is a shallow system with an average depth of less than 5 m and experiences a strong tide with a range of over 4 m and tidal currents that exceed 1 m s^{-1}. The tides in Possession Sound are a combination of semidiurnal and diurnal tides during the spring tide, and this variability leads to prominent periodic stratification. The salinity front is advected by roughly 15 km from Possession Sound into the estuary during the well-mixed strong tides. The longitudinal excursion of the salt wedge during the stably stratified weak tide can reach 8 km.

[6] The lower main stem of the river, roughly 400 m wide, flows southward with Jetty Island to the west, and a secondary connection to the Possession Sound exists at the north end of Jetty Island, which is a bypass consisting of intertidal mudflats (see Figure 1). While in this work we focus on the dynamics in the main channel, *Yang and Khangaonkar* [2008] studied the intertidal marshlands in the distributary channels of the Snohomish system.

[7] Vertical turbulent mixing represents the nonlinear interaction between stratification and vertical shear and thus plays an essential role in the overall flow behavior [*Bowden*, 1981; *Peters*, 1997]. Therefore, care must be taken when parameterizing the eddy viscosity and diffusivity for vertical mixing in numerical models. There are a good number of field-scale simulations for coastal systems that employ two-equation closures and successfully reproduce the observed velocity and salinity/temperature structure [*Kantha and Clayson*, 1994; *Gross et al.*, 1999; *Warner et al.*, 2005a], and turbulence quantities, such as eddy viscosity [*Ilicak et al.*, 2008] and dissipation rate [*Simpson et al.*, 2002; *Stips et al.*, 2002]. Although most studies have found that there is little difference between the performance of the various two-equation closures [*Umlauf and Burchard*, 2005; *Warner et al.*, 2005a, 2005b; *Li et al.*, 2005; *Ilicak et al.*, 2008], very few studies have focused on shallow systems like the Snohomish River estuary in which the flow varies from fully mixed to strongly stratified over tidal time scales.

[8] Given the differences in the physical setting and numerical methods of our application, we compare the results of different two-equation closures and stability functions. This is achieved efficiently using the generic length scale (GLS) framework to implement various two-equation turbulence closures [*Umlauf and Burchard*, 2003].

[9] Using high-resolution model predictions, we explore the temporal variability of turbulence and mixing in the water column at two locations in the estuary, at roughly 6 km and 9 km from the river mouth, respective (Figure 2), and compare the predictions to the field observations [*Giddings et al.*, 2011]. The spatial variability of mixing and the evolution of the salt wedge are investigated along a longi-

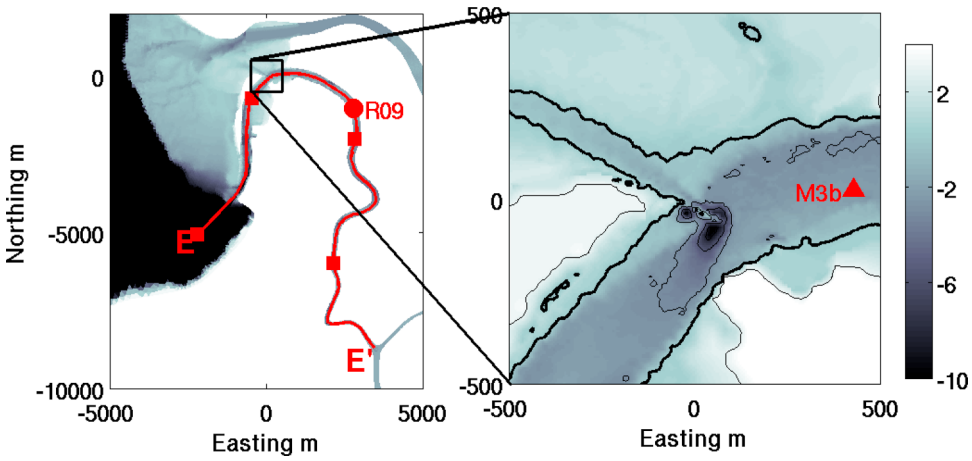

Figure 2. Location of mooring M3b and bathymetry (m above MLLW). Transect E–E' and location R09 are used in discussion of model predictions. The squares along the E–E' transect are for every 5 km from the oceanic end E.

tudinal transect that follows the river centerline. We relate the buoyant production to the change in the potential energy associated with stratification to show the importance of local mixing in the breakdown of the stratification. Finally, we investigate how stratification responds to changes in turbulence with numerical experiments.

[10] This paper presents part of a multiuniversity collaborative effort incorporating remote measurements [*Chickadel et al.*, 2009; *Plant et al.*, 2009], in situ measurements [*Giddings et al.*, 2011] and numerical simulations [*Wang et al.*, 2009] to better understand the dynamics of complex estuarine flows. We focus on the results from the numerical simulations including a detailed comparison to field observations as well as an extended analysis on the turbulent mixing dynamics. While the field observations [*Giddings et al.*, 2011] provide a basic description of the overall dynamics, here we focus on using extensively validated numerical simulation results to address major aspects of the flow that are not resolved by the field data. In section 2 we explain the details of the numerical model, followed by an extensive validation based on mean flow properties and Reynolds stress measurements in section 3. The influence of the turbulence closure scheme in parameterizing vertical mixing is discussed in section 4. We then focus on discussion and interpretation of the temporal (section 5) and spatial (section 6) variability of the stratification and turbulent mixing in the estuary.

2. The Numerical Model

[11] We applied SUNTANS [*Fringer et al.*, 2006] to simulate the hydrodynamics in three dimensions. SUNTANS solves the Navier-Stokes equations with the Boussinesq approximation on a finite volume grid which consists of unstructured, triangular cells in the horizontal and z levels in the vertical. The horizontal velocities are defined as normal to the triangular faces, while vertical velocities are defined at the top and bottom faces of the prismatic cells. The present application builds on the work by *Wang et al.* [2009] with the addition of a generic length scale (GLS) turbulence closure [*Umlauf and Burchard*, 2003] following the implementation of *Warner et al.* [2005b]. The GLS scheme enables implementation of any one of $k-kl$, $k-\epsilon$, or $k-\omega$ closures through changes in a few of the underlying parameters. *Wang et al.* [2009] has described the numerical methods, wetting-drying treatment, and time step constraint of the model. Here, we focus on consideration of the unresolved turbulent mixing and implementation of the turbulence model.

2.1. Reynolds-Averaged Equations

[12] The Reynolds-averaged Navier-Stokes and scalar transport equations contain unclosed terms, namely, the Reynolds stresses $\langle u_i' u_j' \rangle$ and turbulent scalar fluxes $\langle u_j' s' \rangle$. Although exact expressions for the evolution of these correlations can be derived analytically by manipulating the equations, this introduces more unclosed terms such as higher-order correlations of velocity, pressure and scalar fluctuations [*Pope*, 2000].

[13] Alternatively, the Reynolds stresses and the turbulent scalar fluxes can be modeled with the gradient transport hypothesis,

$$-\langle u_i' u_j' \rangle = -\frac{2}{3} k \delta_{ij} + \nu_t \left(\frac{\partial U_i}{\partial x_j} + \frac{\partial U_j}{\partial x_i} \right), -\langle u_j' s' \rangle = \kappa_t \frac{\partial S}{\partial x_j}, \quad (1)$$

where ν_t is the eddy viscosity and κ_t is the eddy diffusivity, $U_i = \langle u_i \rangle$ are the time-averaged velocities, $S = \langle s \rangle$ is the time-averaged scalar concentration, and k is the turbulent kinetic energy (TKE). For shallow flows which possess restricted vertical length scales, the cross derivatives in the Reynolds stresses (e.g., $\partial^2/\partial x \partial z$) can be neglected, and the horizontal eddy viscosity and diffusivity can be parameterized as constants. Similar treatments that parameterize the horizontal and vertical turbulent processes anisotropically are applied in many coastal flow models, e.g., TRIM3D [*Casulli and Cattani*, 1994], ROMS [*Shchepetkin and McWilliams*, 2005], FVCOM [*Chen et al.*, 2003], etc. Because *Wang et al.* [2009] demonstrated that nonhydrostatic effects are negligible in estuarine-scale hydrodynamics, the simulations presented here assume that the flow is hydrostatic. Employing the aforementioned turbulence

model, the primitive momentum equations and scalar transport equations simulated by SUNTANS are given by

$$\frac{\partial U}{\partial t}+\nabla\cdot(\mathbf{U}U)-fV=-\frac{1}{\rho_0}\frac{\partial p}{\partial x}+\nabla_H\cdot(\nu_H\nabla_H U)+\frac{\partial}{\partial z}\left((\nu_t+\nu)\frac{\partial U}{\partial z}\right), \quad (2)$$

$$\frac{\partial V}{\partial t}+\nabla\cdot(\mathbf{U}V)+fU=-\frac{1}{\rho_0}\frac{\partial p}{\partial y}+\nabla_H\cdot(\nu_H\nabla_H V)+\frac{\partial}{\partial z}\left((\nu_t+\nu)\frac{\partial V}{\partial z}\right), \quad (3)$$

$$\frac{\partial S}{\partial t}+\nabla\cdot(\mathbf{U}S)=\nabla_H\cdot(\kappa_H\nabla_H S)+\frac{\partial}{\partial z}\left((\kappa_t+\kappa)\frac{\partial S}{\partial z}\right), \quad (4)$$

where $\mathbf{U}$ is the velocity vector, p is the hydrostatic pressure, ν is the background viscosity and κ is the background diffusivity. The horizontal eddy viscosity ν_H and eddy diffusivity κ_H are set to be 10^{-4} m^2 s^{-1} as *Wang et al.* [2009] show there is sufficient numerical diffusion to account for unresolved horizontal turbulent motions. The horizontal gradient operator is given by $\nabla_H = \frac{\partial}{\partial x}\mathbf{e_x} + \frac{\partial}{\partial y}\mathbf{e_y}$, and the vertical velocity is obtained via the continuity equation

$$\frac{\partial W}{\partial z}=-\nabla_H\cdot\mathbf{U}_H, \quad (5)$$

where $\mathbf{U}_H$ is the horizontal velocity vector. In our model we ignore the effects of temperature on the dynamics since it plays a relatively minor role in influencing the density, and we use the linear equation of state $\rho=\rho_0(1+\beta s)$, where $\beta = 7\times10^{-4}$ psu^{-1} is the saline expansivity.

2.2. Turbulence Closure

[14] *Umlauf and Burchard* [2003] proposed a generic length scale (GLS) approach to unify many two-equation closures with one set of equations. We implemented this algorithm in SUNTANS following *Umlauf and Burchard* [2003] and *Warner et al.* [2005b]. Using the turbulent kinetic energy (TKE) k and a turbulent macroscale l, the GLS method defines a length scale parameter $\psi=(C_\mu^0)^p k^m l^n$. Varying the coefficients p, m, n and other constants results in traditional standard closures such as $k-kl$ or $MY2.5$ [*Mellor and Yamada*, 1982], $k-\epsilon$ [*Rodi*, 1987], $k-\omega$ [*Wilcox*, 1988], etc. The partial differential equations governing the behavior of k and ψ are given by

$$\frac{\partial k}{\partial t}+\nabla\cdot(\mathbf{U}k)=\frac{\partial}{\partial z}\left(\frac{\nu_t}{\sigma_k}\frac{\partial k}{\partial z}\right)+P+B-\epsilon, \quad (6)$$

$$\frac{\partial \psi}{\partial t}+\nabla\cdot(\mathbf{U}\psi)=\frac{\partial}{\partial z}\left(\frac{\nu_t}{\sigma_\psi}\frac{\partial \psi}{\partial z}\right)+\frac{\psi}{k}(c_1P+c_3B-c_2\epsilon F_{wall}), \quad (7)$$

where P and B are the rate of shear and buoyant production (termed as destruction when $B<0$), respectively, and are defined as

$$P=\max(\nu_{\min},\nu_t)M^2,\ B=-\max(\kappa_{\min},\kappa_t)N^2, \quad (8)$$

where

$$M^2=\left(\frac{\partial U}{\partial z}\right)^2+\left(\frac{\partial V}{\partial z}\right)^2,\ N^2=-g\beta\frac{\partial S}{\partial z}. \quad (9)$$

[15] Assuming proportionality of the turbulent energy cascade, the dissipation rate ϵ is given by

$$\epsilon=\left(C_\mu^0\right)^3 k^{3/2}l^{-1}. \quad (10)$$

[16] The wall function F_{wall} is used for the $k-kl$ (i.e., MY2.5) closure scheme and is set to unity for the other closures. We employ the wall function for open channel flow as suggested by *Blumberg et al.* [1992] which produces a symmetric eddy viscosity profile.

[17] The coefficients are specified in the notation section. The model includes the effects of local production, dissipation, buoyancy and transport of k and ψ. The background eddy viscosity and diffusivity are given by $\nu_{\min}$ and $\kappa_{\min}$, respectively, and these represent unresolved processes such as shear instabilities, and help turbulent kinetic energy grow in an initially nonturbulent flow field [*Monismith and Fong*, 1996]. In our model, the background values $\nu_{\min}$ and $\kappa_{\min}$ are not included in ν_t and κ_t, and thus the notation is different from that given by *Warner et al.* [2005b]. We set $\nu_{\min}=\nu$ and $\kappa_{\min}=\nu\kappa_t/\nu_t$, which ensures a correct turbulent Prandtl number and a reasonable B/ϵ ratio during strong stratification. After k and l are computed with equations (6) and (7), ν_t and κ_t are then obtained with the stability functions.

[18] We incorporated the KC [*Kantha and Clayson*, 1994] and Canuto-A (CA) [*Canuto et al.*, 2001] stability functions and discuss the differences between the two in this paper.

[19] One important property of the KC stability functions is that they yield a critical Richardson number (Ri_c) of roughly 0.2, whereas the CA stability functions give $Ri_c\sim1$, which may be crucial for correctly reproducing the development and breakdown of the salt wedge in the present simulations. More detail on the formulations of these stability functions can be found in the work of *Warner et al.* [2005b].

2.3. Numerical Methods for GLS

[20] The transport of k and ψ are solved via the finite volume scalar transport routine in SUNTANS (see details given by *Fringer et al.* [2006]) with the addition of local source terms and boundary fluxes at the top and bottom of the water column. The addition of the dissipation as a source term may yield instabilities and thus it is treated implicitly. Following the approach in *Deleersnijder et al.* [1997] and *Umlauf and Burchard* [2003], the buoyancy term is solved differently depending on the sign of $P+B$. When $P^n+B^n\geq0$, the TKE equation (6) is discretized with

$$\frac{k^{n+1}-k^n}{\Delta t}+\nabla\cdot(\mathbf{u}^n k^n)=\frac{\partial}{\partial z}\left[\frac{\nu_t^n}{\sigma_k}\left(\frac{\partial k}{\partial z}\right)^{n+1}\right]+(P^n+B^n)-\epsilon^n\frac{k^{n+1}}{k^n}, \quad (11)$$

where the variable n implies the time step and is not to be confused with the parameter n in the GLS implementation.

Table 1. Coefficients Used in $k-kl$, $k-\epsilon$, and $k-\omega$ With KC and CA Stability Functions

	$k-kl$	$k-\epsilon$	$k-\omega$
p	0.0	3.0	−1.0
m	1.0	1.5	0.5
n	1.0	−1.0	−1.0
σ_k	2.44	1.0	2.0
σ_ψ	2.44	1.3	2.0
c_1	0.9	1.44	0.555
c_2	0.5	1.92	0.833
c_3^{+}[a]	1.0[b]	1.0	1.0
c_3^{-}[a] (KC)	2.53[b]	−0.41	−0.58
c_3^{-}[a] (CA)	2.38[b]	−0.63	−0.64
C_μ^0 (KC)	0.5544	0.5544	0.5544
C_μ^0 (CA)	0.5270	0.5270	0.5270
c (KC)	1.0	1.0	1.0
c (CA)	$\sqrt{2}(C_\mu^0)^3$	$\sqrt{2}(C_\mu^0)^3$	$\sqrt{2}(C_\mu^0)^3$

[a]When $B > 0$, $c_3 = c_3^{+}$, and when $B < 0$, $c_3 = c_3^{-}$.
[b]The c_3 values for $k-kl$ are different from original MY2.5 ($c_3 = 0.9$), shown to perform better in wind-driven mixed layer test [*Warner et al.*, 2005b].

Because equation (11) is solved after the free surface is updated at each time step, the values of the vertical grid spacing at the new time step (Δz^{n+1}) are used to compute vertical derivatives. When $P + B < 0$, equation (6) is discretized with

$$\frac{k^{n+1}-k^n}{\Delta t}+\nabla\cdot(\mathbf{u}^n k^n)=\frac{\partial}{\partial z}\left[\frac{\nu_t^n}{\sigma_k}\left(\frac{\partial k}{\partial z}\right)^{n+1}\right]+P^n-(-B^n+\epsilon^n)\frac{k^{n+1}}{k^n}. \tag{12}$$

[21] The discretization of equation (7) for ψ is treated in a similar manner.

[22] We implemented the flux boundary conditions described by *Warner et al.* [2005b] for the vertical diffusion term, which are derived by assuming the viscous sublayer is not resolved and the boundary is within the universal "log law" region of the wall [*Burchard and Petersen*, 1999; *Jones*, 1994]. The fluxes are input at the top and bottom finite volume faces. No-flux conditions are applied at the top and bottom for k, and the boundary fluxes for ψ at the bottom (subscript b) and the free surface (subscript s) are given by

$$\left(\frac{\nu_t}{\sigma_\psi}\frac{\partial\psi}{\partial z}\right)_b=n\frac{\nu_t}{\sigma_\psi}\left(C_\mu^0\right)^p k^m(\kappa_{VK})^n\Delta z_b^{n-1},$$
$$\left(\frac{\nu_t}{\sigma_\psi}\frac{\partial\psi}{\partial z}\right)_s=-n\frac{\nu_t}{\sigma_\psi}\left(C_\mu^0\right)^p k^m(\kappa_{VK})^n\Delta z_s^{n-1}, \tag{13}$$

where Δz_b and Δz_s are the bottom and top layer thickness, respectively, and the other parameters are defined in Table 1. We found that this boundary condition yields better results than a Dirichlet boundary condition when tested with idealized cases. However, because the calculation involves negative powers of the layer thickness (except for the $k-kl$ model, for which $n = 1$), instability develops when the layer thickness becomes very thin in the presence of wetting and drying. Therefore, we set minimal thickness of $\Delta z_b = 10\%$ and $\Delta z_s = 50\%$ of the initial layer thickness. Our implementation of the GLS model has been validated with open channel flow, wind-induced mixed layer deepening, and idealized estuary test cases, all of which yield consistent results with those in the work by *Warner et al.* [2005b]. In the present results, the $k-kl$ form of GLS scheme with CA stability functions are employed except when we specifically compare the results of different closure schemes.

[23] To quantify the model errors, we adopt the model skill score defined by *Murphy* [1988], which is the ratio of the root-mean-square error normalized by the standard deviation of the observation,

$$\mathrm{SS}=1-\frac{\sum(X_{\mathrm{model}}-X_{\mathrm{obs}})^2}{\sum\left(X_{\mathrm{obs}}-\overline{X_{\mathrm{obs}}}\right)^2}, \tag{14}$$

where X is the variable being evaluated and $\overline{X}$ is the temporal average. Such a metric allows for comparison between different models and is used by *Allen et al.* [2007], *Stow et al.* [2009], and *Ralston et al.* [2010], and a skill score greater than 0.65 indicates an excellent prediction [*Allen et al.*, 2007]. *Ralston et al.* [2010] compared a variety of metrics and found that metric *SS* is a better indicator of model performance than the widely used model skill (MS) metric defined by *Wilmott* [1981] which is employed by, among others, *Warner et al.* [2005a], *Li et al.* [2005], and *Ralston et al.* [2008]. We apply the skill score metric to the Reynolds stress for the first time and it is worth noting that Reynolds stress varies by orders of magnitude and the skill score defined above represents the errors in the peak values at its best. It is also found that the value is sensitive to the treatment of noise, and thus, should be only used as a reference.

3. Snohomish River Estuary Model Validation

[24] The computational domain of the model includes the Snohomish River main channel, a simplified tributary channel, Possession Sound and Port Susan Bay to the north of Possession Sound. The horizontal mesh is shown in Figure 3. Triangles with edge lengths of 8–35 m resolve the main river channel, while stretching is employed to expand the triangle edge lengths to 300 m in the sound. Vertical resolution is 0.2–0.3 m in the top 20 m. For layers below 20 m existing in the deeper offshore area, grid stretching is employed at a rate of 118% moving downward from one z level to the next. Tidal boundaries are on the west side of Possession Sound and forced with estimated tidal fluxes. The bottom drag is parameterized with a bottom roughness height of 2.5×10^{-4} m and is derived from the field observations. *Wang et al.* [2009] describe more details related to the computational domain, bathymetry, boundary conditions, and initial conditions. That work also includes model validation based on free surface in the sound, at a mooring in the main channel and at an upstream gage station, as well as depth-averaged velocities at two mooring sites in the main channel and in the bypass channel, respectively. Discussion is also made regarding model sensitivity to bathymetry, bottom drag, momentum advection, nonhydrostatic pressure, and fresh river flow.

[25] In the present application, we made changes to that in the work by *Wang et al.* [2009] to reflect more accurate and realistic boundary and initial conditions. Specifically, we improve the channel geometry at the upstream bifurcation of the Snohomish River and the tributary channel (Figure 3)

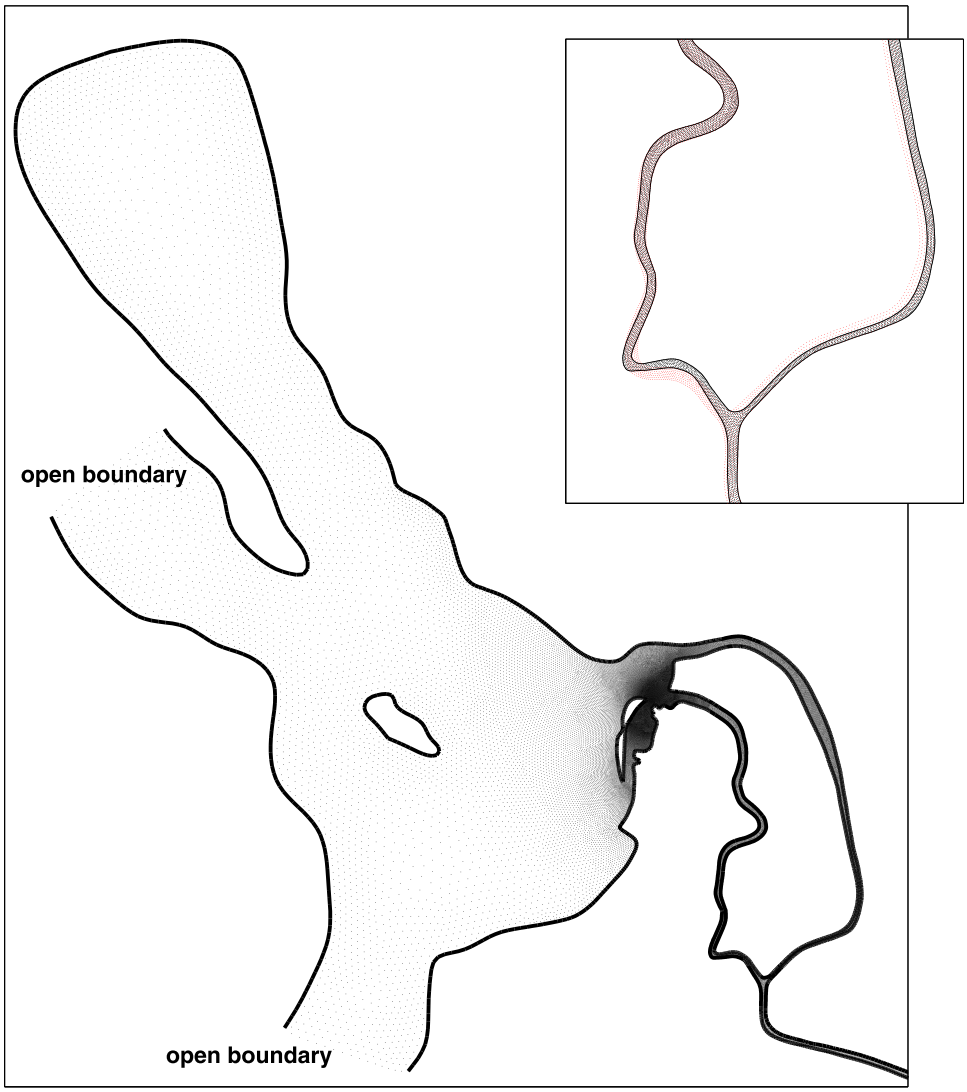

Figure 3. The unstructured grid used in the simulations. Cell centers are shown for clarity. The embedded window illustrates the difference between the grid used by *Wang et al.* [2009] (red) and the current work (black).

based on nautical charts. We also incorporated along-channel bottom elevation measured by *Chickadel et al.* [2009] in the upstream portion of the river, which was approximated as a constant bottom slope by *Wang et al.* [2009]. To improve the no-stratification approximation of Possession Sound in *Wang et al.* [2009], weak background stratification (27 psu near the top and 30 psu at depth) is applied in Possession Sound based on the profile measured by *Fram et al.* [2003] at a similar low-flow period. While the most notable effect of these changes is to improve the salinity prediction during LLW, which is now 3 psu lower than that in the work by *Wang et al.* [2009] when using the same turbulence model as in the work by *Wang et al.* [2009] ($k - kl$). This only improves the model skill for the bottom salinity by less than 0.05 and the model skill for free surface and velocities by much less than this amount. Given the favorable match to observations, model parameters were not tuned to improve model performance. In what follows we avoid discussion of model sensitivity to changes in parameters and focus only on validation with mooring data in the main channel.

[26] The multiple moorings of our field program [*Giddings et al.*, 2011] were located within 2 km of a sill near the tip of Jetty Island in the Snohomish River to provide a detailed picture of the near-field dynamics around the sill. Because the distance between the moorings is orders of magnitude smaller than the tidal wavelength, the tidal-scale hydrodynamics at each mooring is similar. However, some moorings show more high-frequency variability due to disturbances from local features such as the channel bifurcation, pilings near the river banks, separation over the sill, etc. Owing to its weakest local perturbations, we chose to validate our model with observations from mooring M3b (for location see Figure 2), although it is still to some extent influenced by the flow through the bypass, which is controlled by the wetting and drying of intertidal mudflats [see *Wang et al.*, 2009]. The small-scale flow features and mixing patterns associated with this flow are not fully

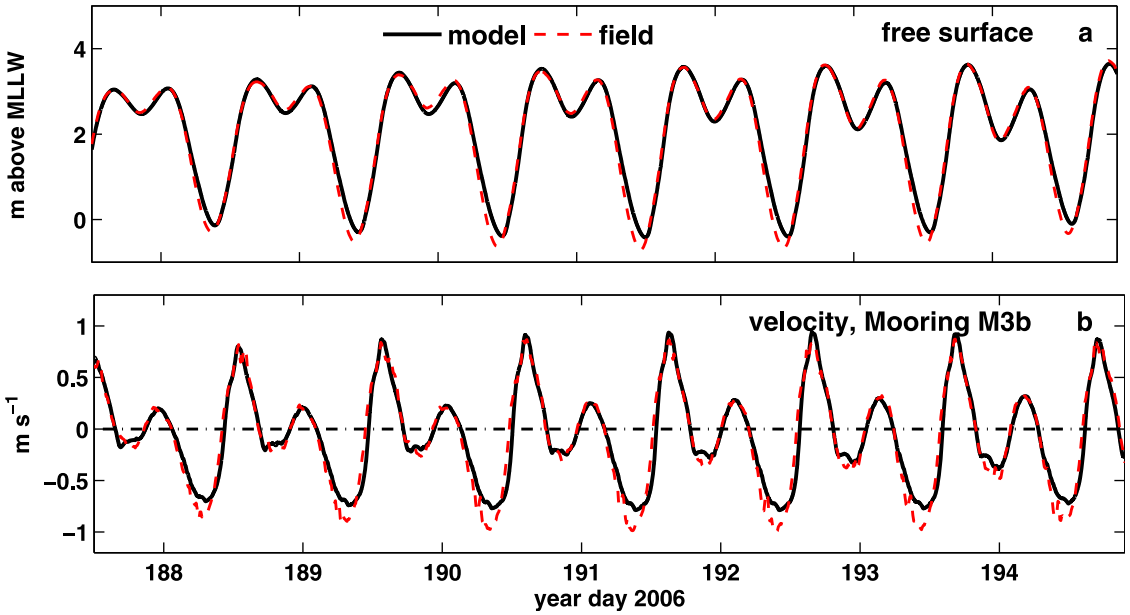

Figure 4. Time series of (a) free surface height at mooring site M3b and (b) depth-averaged along-channel velocity at mooring site M3b.

understood and need to be further investigation and validated with improved bathymetry and roughness, which we leave to a future manuscript. Accuracy of the model in simulating these features is not crucial to obtaining reasonable predictions of the estuarine-scale hydrodynamics.

[27] Figure 4 compares the free surface height and the depth-averaged along-channel velocity with the in situ observations at the mooring M3b. Year day 190 is 9 July 2006. These results do not have notable difference from those given by *Wang et al.* [2009]. Overall, the predictions compare favorably with the measurements. The predicted water level at lower low water is still slightly higher than the observations, and the observed peak ebb flow is systematically weaker but lasts longer than the observations.

3.1. Vertical Structure of Velocity and Salinity

[28] During the spring tide, the tidal forcing consists of strong diurnal and semidiurnal constituents. A strong ebb and flood (herein, referred to as strong tide) occurs following a weak ebb and flood (herein referred to as weak tide) over a diurnal cycle. The strong tide features an amplitude of over 3 m and peak depth-averaged velocity of over 1 m s^{-1}, while the weak tide has an amplitude of less than 2 m and peak depth-averaged velocity of less than 0.4 m s^{-1}.

[29] Figure 5 illustrates the vertical structure of the along-channel velocity at mooring site M3b from the model and the field measurements, and Figure 6 shows the time series of top and bottom salinity and bottom-top difference to indicate the degree of stratification. The top and bottom salinity measurements were taken at location z_1 at roughly 1 m below the free surface, z_2 at roughly 2 m below free surface, and z_3 at roughly 0.2 m above the bottom, and model predictions were interpolated to the same vertical locations for the comparison. The model captures the velocity structure very well in both amplitude and phase and obtains a skill score of 0.92. The salinity predictions span a wide range of salinity and stratification conditions and are generally in good agreement with the measurements during this period. The skill scores are 0.86 for the top salinity, 0.92 for the bottom salinity and 0.62 for the top-bottom salinity difference. Periodically stratified conditions are present in which the water column is strongly stratified during the weak tide and is relatively well mixed during the strong tide with the flow being fresh for a short period of time.

[30] The predicted onset and breakdown of stratification occur with correct timing and magnitude. The model overpredicts the stratification near the end of strong flood due to an overprediction of the strength and freshness of the flow from the bypass.

[31] For a more quantitative comparison to the field observations, the profiles of the velocity and salinity during different stages of the tide are depicted in Figure 7, which shows that the model reproduces the main features in the observed flow reasonably well. During the strong ebb and early stages of the strong flood, the stratification is weak and the velocity profile resembles the logarithmic profile in an open channel flow (profiles a, b, and i in Figure 7). Baroclinic effects become notable at the end of the strong flood (profile c in Figure 7) because the presence of barotropic flow is relatively weak and the greater depth favors the development of gravitational circulation. During ebb tide, the combined effects of tidal straining and gravitational circulation induce a linear velocity profile (profiles d and e in Figure 7) with a strong vertical gradient at all depths, while the velocity profile during flood tide (profile f in Figure 7) has a maximum at an intermediate depth, which is similar to the observations of *Geyer and Farmer* [1989] in a similar system. The salinity is first weakly stratified over the water column (profiles c and d in Figure 7) and later develops a sharper gradient near the free surface when the stratification becomes stronger (profiles e–g in Figure 7). These results indicate that, likely owing to numerical diffusion, the model tends to underpredict vertical gradients of

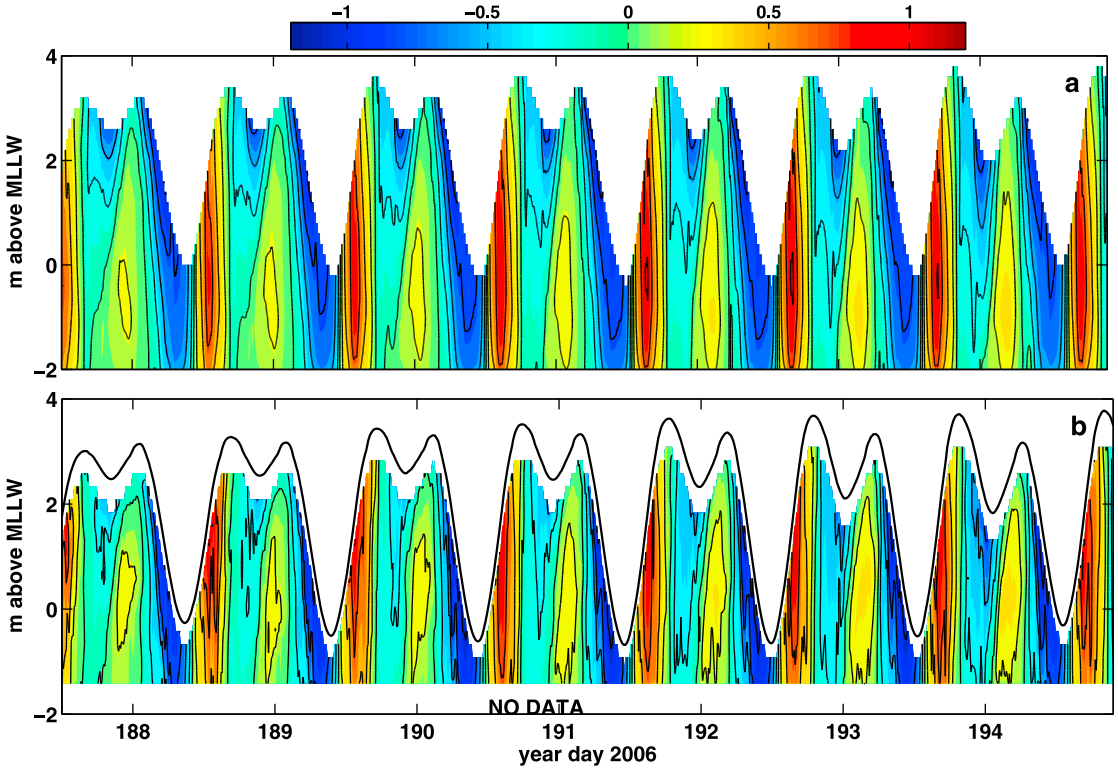

Figure 5. Vertical profile (m s^{-1}) of along-channel velocity at M3b: (a) prediction and (b) measurements. Measurements are unavailable very close to the surface and the bottom. Positive velocity is defined in the upstream direction (flood). For clarity, only part of the entire simulation period is shown.

velocity and salinity throughout much of a tidal cycle. Although higher-order methods for advection of momentum and scalars may reduce the numerical diffusion, they are difficult to implement and not well behaved in the presence of strong wetting and drying. Overall, however, the model has correctly represented the primary variability in the vertical structure.

3.2. Richardson Number

[32] A bulk Richardson number is calculated for the upper portion of the water column using the locations of the upper two salinity observations which are located at $z_1 = 1$ m below the free surface and $z_2 = 2$ m below the free surface. Using values at these two locations indicated by the appropriate subscripts (e.g., s_1 is the observed salinity over time at $z = z_1$), the bulk Richardson number is given by

$$Ri_b = \frac{N_b^2}{M_b^2}, \tag{15}$$

where

$$N_b^2 = -g\beta\left(\frac{s_1 - s_2}{\Delta z}\right), M_b^2 = \left(\frac{u_1 - u_2}{\Delta z}\right)^2 + \left(\frac{v_1 - v_2}{\Delta z}\right)^2, \tag{16}$$

where $\Delta z = z_1 - z_2$ is the vertical distance between the two salinity measurements. All observations and predictions are interpolated in both time and space to vertical locations z_1 and z_2 at the time of the salinity measurements.

[33] Figure 8 depicts a comparison between predicted and observed values of Ri_b, N_b^2 and M_b^2. The bulk Richardson number is normalized by the canonical value of the gradient Richardson number of $Ri_c = 0.25$ [*Miles*, 1961]. The results show that the model captures the variability of Ri_b quite well during the spring tide (periodic stratification), in that Ri_b/Ri_c is well below unity during the strong tide and remains roughly at unity during the stratified weak tide. During periods of stable stratification, Ri_b/Ri_c varies in the vicinity of 2 both in the predictions and in the observations.

[34] Figure 8 indicates that Ri_b is predicted fairly accurately, while M_b^2 and N_b^2 are both slightly underpredicted during the stratified weak tide due to the underprediction of the gradients. Because the bulk Richardson number varies by orders of magnitude and approaches infinity during slack tide, interpretation of a model skill is difficult and so we do not compute it in this manuscript.

3.3. Reynolds Stress

[35] The Reynolds stress is a key turbulence measurement because TKE, k, turbulence macroscale, l, production, P, dissipation, ϵ and buoyant production, B, can all be estimated using Reynolds stresses $\langle u'w' \rangle$ and $\langle v'w' \rangle$, mean flow quantities from scaling arguments and a local balance assumption.

[36] Figure 9 compares the predicted and measured magnitude of the Reynolds stress with a time series of the values at a near-bottom depth shown in Figure 9c for a more quantitative comparison. The Reynolds stresses in the observations are computed following the variance technique described by *Stacey et al.* [1999b], and the magnitude is computed as $\sqrt{\langle u'w' \rangle^2 + \langle v'w' \rangle^2}$, while in the model it is

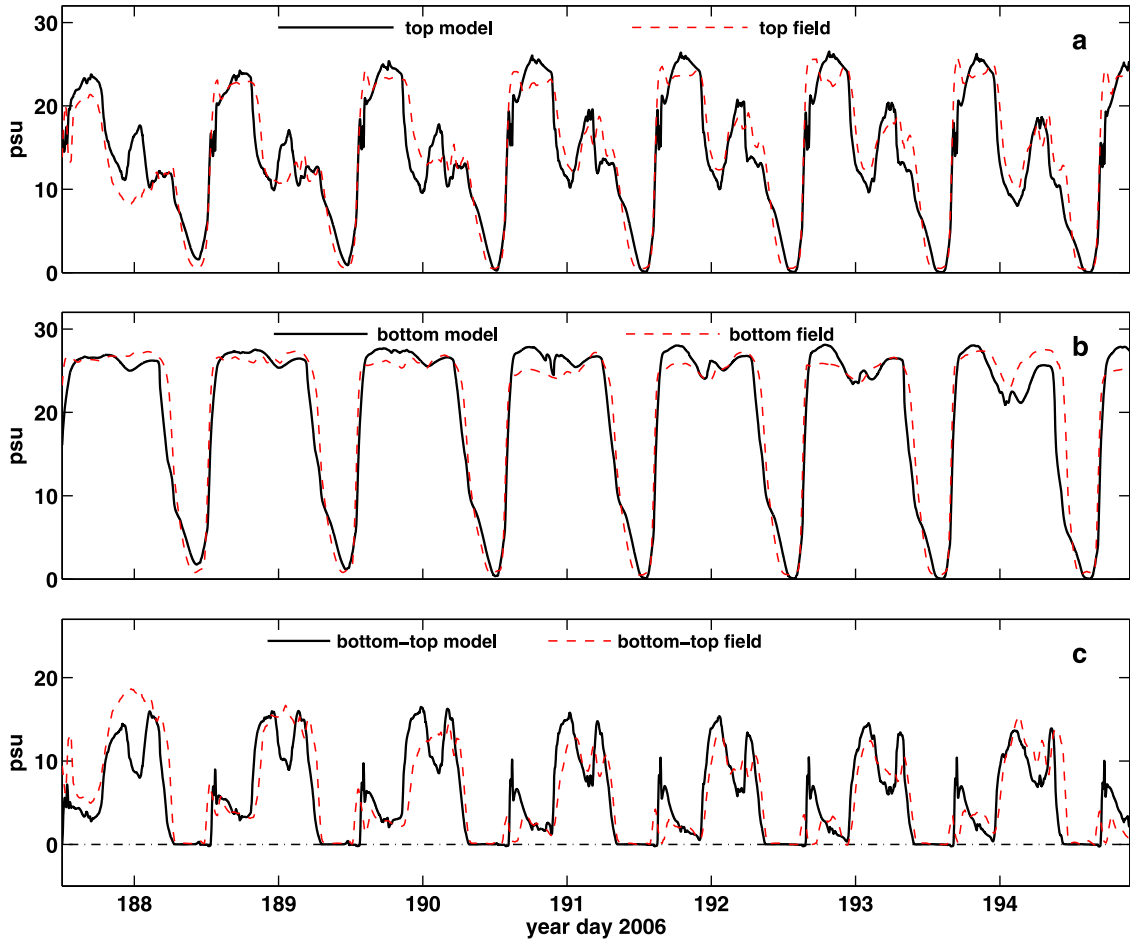

Figure 6. Time series of (a) top and (b) bottom salinity and (c) bottom-top salinity difference at mooring site M3b. For clarity, only part of the entire simulation period is shown.

computed as $\nu_t M$ from the predictions. The near-bottom location is the depth of the bottommost ADCP bin (roughly 1 m above the bed), and the model prediction is interpolated to the same vertical location. It is important to note that the near-bottom Reynolds stress here is not equivalent to the bottom shear stress imposed at the bottom boundary of the momentum equation, which is parameterized with the quadratic drag law [see *Wang et al.*, 2009].

[37] In general, the predicted and measured Reynolds stress show similar behavior and give a skill score of 0.21 (data values lower than the noise floor of 1e-4 m^2 s^{-1} are set to zero). The peak Reynolds stresses occur during the strong ebb and flood, and the model demonstrates a linear vertical profile in the Reynolds stress which is a common feature of steady, unstratified open channel flow. The near-bottom Reynolds stress is underpredicted for the strong ebb (Figure 9c) which consistently occurs at multiple mooring sites (not shown). The reason might be that during the strong ebb, the velocity gradients near the bottom and shallow shoal are greater than those during strong flood, and numerical diffusion leads to more significant energy dissipation near the bottom and shoals.

[38] For the strong flood, the peak stress is overpredicted (Figure 9c) at mooring M3b, which is not a persistent pattern at all locations (not shown) and it is yet unclear what is responsible for the errors.

[39] The observations show that during the strong ebb there is a short sharp peak before the main peak in the near-bottom stress, e.g., around day 193.3 and 194.4, and this is associated with a thin layer of elevated interfacial turbulence roughly along the 10 psu isohaline near the front end of the salt wedge. This feature is not well captured by the model.

[40] Later in the strong flood, a two-layer structure is present in the predicted Reynolds stress corresponding to the confluent buoyant fluid from the bypass. The signal is not as strong in the observations although it is more evident some of the time, e.g., around day 193.7. The weaker signal in the observations occurs because the model overpredicts the strength and freshness of the bypass flow (mentioned earlier). Finally, the observations show large Reynolds stress magnitudes near the free surface, which is not likely to be related to wind because this effect is not manifested at a mooring nearby [*Giddings et al.*, 2011]. During the subsequent weak tide, the Reynolds stress is overall weak. Little turbulence activity occurs above the noise level of the measurements.

4. Turbulence Closures for Vertical Mixing

[41] We tested the $k - kl$, $k - \epsilon$, and $k - \omega$ models in combination with the *CA* [*Canuto et al.*, 2001] and *KC* [*Kantha and Clayson*, 1994] stability functions and use the

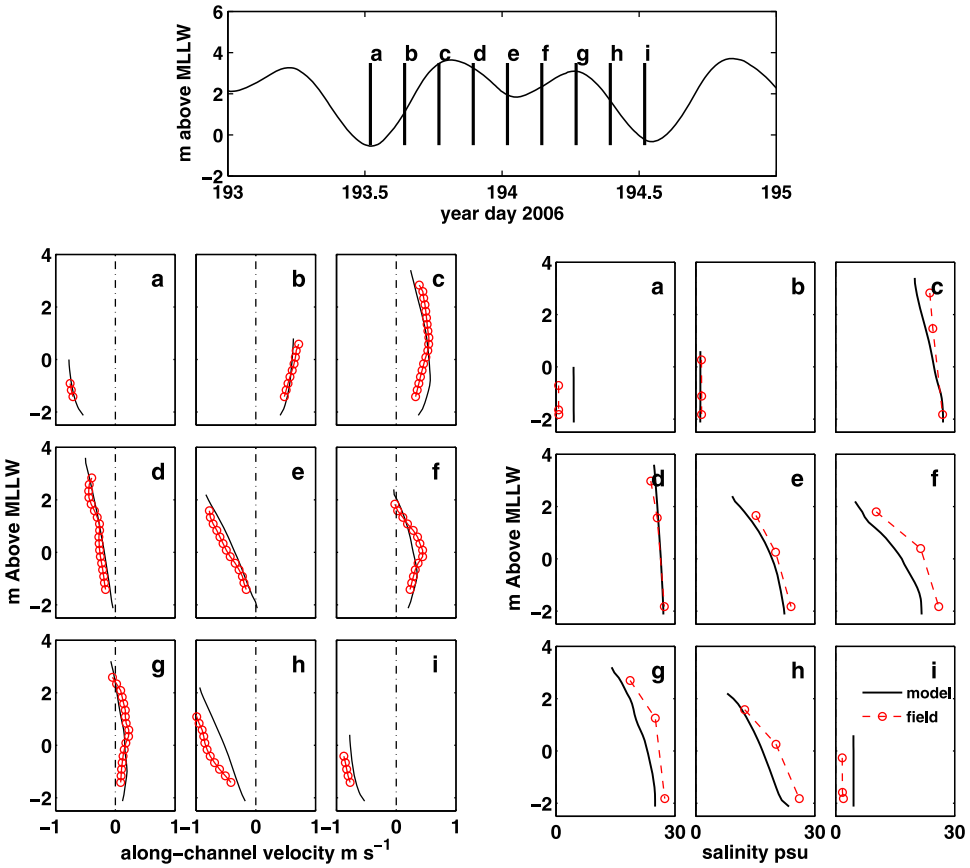

Figure 7. Comparison of the vertical profiles of (left) velocity and (right) salinity at mooring site M3b during different stages of a spring tidal cycle. The time stamps are depicted at the top.

results to compare the spatiotemporal features of the predictions for these various closures. Several studies present an evaluation of the performance of these closures and found no major differences among them [*Umlauf and Burchard*, 2005; *Warner et al.*, 2005b; *Li et al.*, 2005; *Ilicak et al.*, 2008; *Liu et al.*, 2009]. However, to our knowledge, few of the previous comparisons of two-equation turbulence closures were performed in a similar nonlinear, shallow, tidal system with strongly variable stratification.

[42] Figure 10 presents a comparison of the predicted top, bottom and bottom-top salinity difference, as well as the vertical profile of velocity and salinity at day 193 from several combinations of the closures. In general, the effect of the stability functions is more significant than the effect of the closure scheme. In the test of the $k-kl$ closure with the KC stability functions, the model fails to predict the fresh flow at low tide. The minimum salinity is roughly 3 psu, which is similar to the results obtained by *Wang et al.* [2009], who employ the G88 [*Galperin et al.*, 1988] stability functions, which are similar to the KC functions. Using $k-kl$ with KC, the vertical shear and salinity gradient are stronger than the other cases. This is consistent with the fact that the KC stability functions are associated with a lower critical Richardson number than the CA stability functions, and thus the KC stability functions tend to predict more stable stratification and stronger baroclinic circulation, which leads to stronger salt intrusion into the estuary. The KC stability functions also lead to an earlier onset and later breakdown of the stratification over a tidal cycle.

[43] The differences between the closure schemes are relatively minor when the same CA stability functions are applied. The $k-\omega$ scheme appears to predict slightly weaker vertical gradients, stratification and salt intrusion than other schemes. The $k-kl$ and $k-\epsilon$ schemes perform very similarly while $k-\epsilon$ predicts greater gradients near the free surface.

[44] One might expect that small differences between the closure schemes should accumulate over time and yield more significant differences after several tidal cycles. However, strong tidal advection flushes the estuary and effectively resets the system at the end of each diurnal tidal cycle, which appears to diminish the differences between the closures. The skill scores for salinity, velocity and Reynolds stress predictions at mooring site M3b from the tested closure schemes and stability functions are listed in Table 2.

[45] Figure 11 illustrates the salinity and TKE distributions along transect E–E' (see Figure 2) at an instant during the weak flood. Figure 11 shows that the $k-\omega$ closure predicts slightly stronger turbulence along the entire salt wedge than other closures.

[46] The salt front intrusion (indicated by the 5 psu salinity contour) is 0.5 km seaward of that with the $k-kl$ and $k-\epsilon$ closure schemes, and the near-bottom salinity is consistently weaker along the salt wedge, as is the vertical

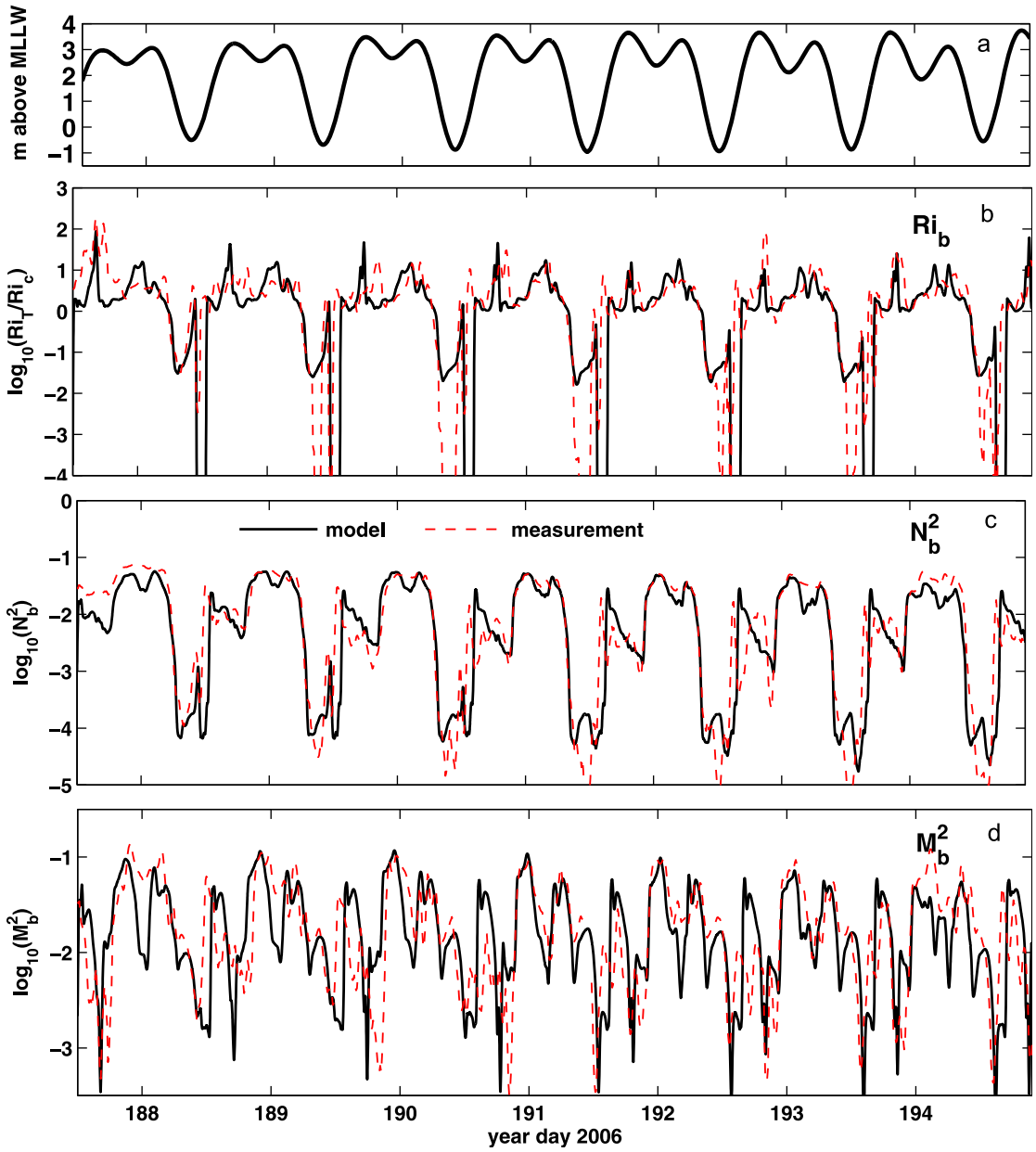

Figure 8. (a) The tidal signal. Comparison of observed to predicted (b) bulk Richardson number (equation (15)), (c) the buoyancy frequency squared, N_b^2 (equation (16)), and (d) the strain rate squared, M_b^2 (equation (16)) at mooring site M3b.

gradient of salinity. As expected, the differences between the CA and KC stability functions are more notable.

[47] The KC stability functions (Figure 11d) predict a thinner bottom mixed layer and weaker turbulence in a thicker upper layer (Figure 11h). They also result in a greater predicted horizontal extent of the salt wedge and a sharper vertical salinity gradient along the isopycnals. This leads to stronger salt intrusion by a distance of 1 km over the next largest intrusion which results from use of $k-\epsilon$ (Figure 11b).

[48] In summary, the GLS model appears to work robustly and the closures are shown to perform very similarly and the CA stability functions give better results than the KC stability functions for the large-scale mixing dynamics.

[49] For the discussion in the remainder of this paper we present results from the $k-kl$ model with the CA stability functions since the $k-kl$ model behaves best with the boundary conditions that are specific to the SUNTANS implementation. Small, unphysical fluctuations appear in other closures, most significantly with $k-\epsilon$, when the free surface fluctuates between layers or becomes dry because of the negative power on the layer thickness (see equation (13)) when calculating the boundary flux.

[50] This does not imply that the $k-kl$ model is the model of choice in general for simulations of coastal flows, and may not perform as well under certain conditions [*Umlauf et al.*, 2003], such as in the presence of wind. One of the well-known limitations of the $k-kl$ model is that it requires

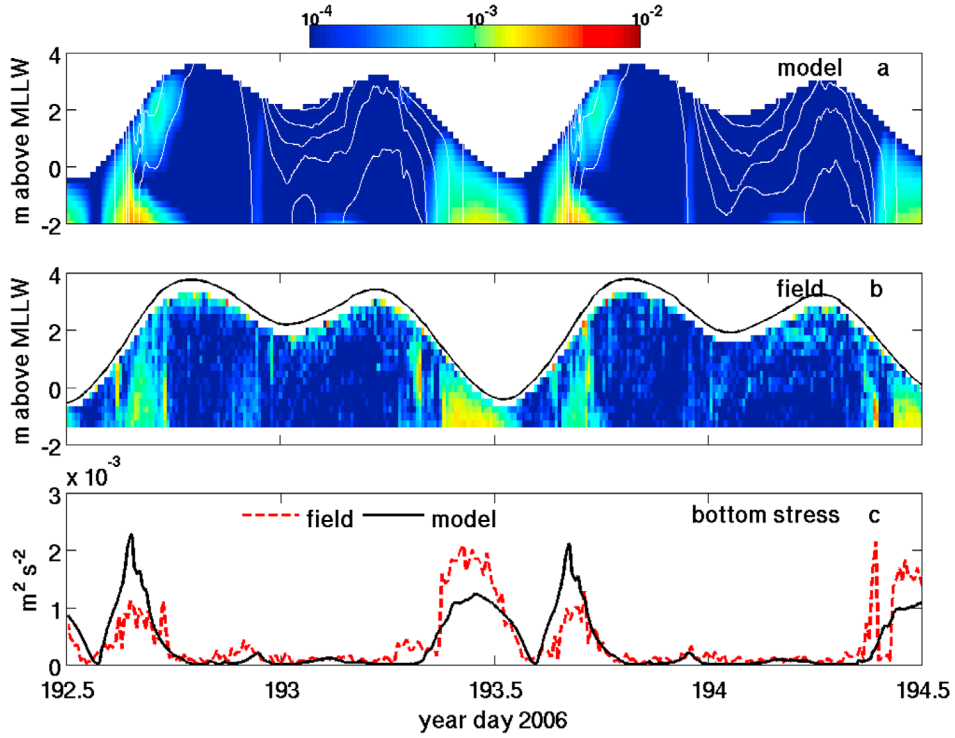

Figure 9. Time series of the Reynolds stresses (m^2 s^{-2}) in the water column at mooring site M3b: (a) model prediction, (b) field measurements, and (c) comparison of the bottom stress at the bottommost ADCP bin. Salinity contours are plotted for every 4 psu in Figure 9a.

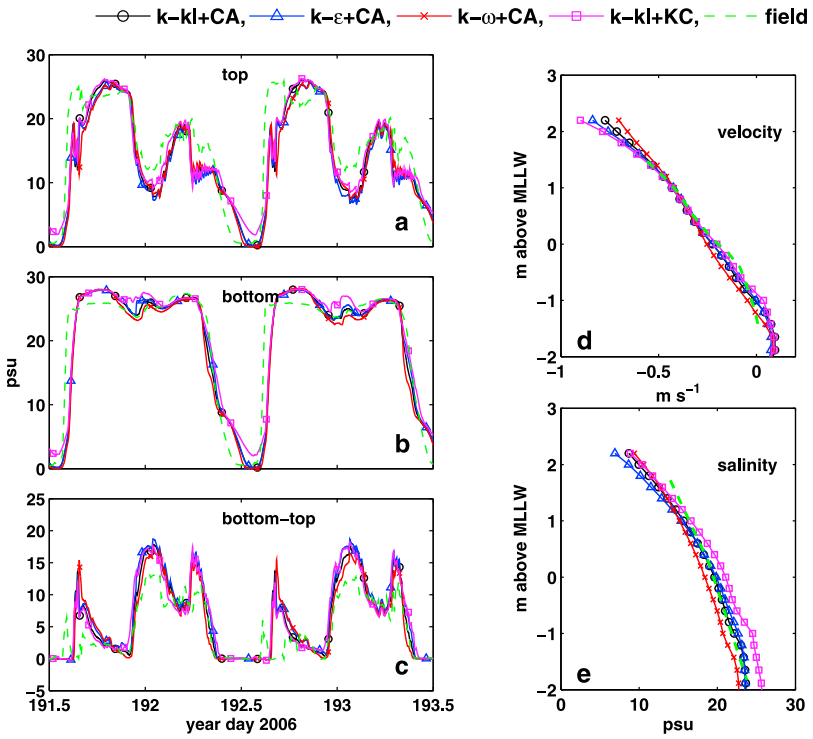

Figure 10. (a–c) Time series of salinity predictions at mooring site M3b, (d) vertical velocity, and (e) salinity profiles at year day 193 from different combinations of closure schemes and stability functions.

Table 2. Skill Scores for Salinity, Along-Channel Velocity, and Reynolds Stress Predictions at Mooring M3b From Different Turbulence Closure Schemes and Stability Functions

	Top Salinity	Bottom Salinity	Bottom-Top Difference	Along-Channel Velocity	Reynolds Stress
$k-kl$ + CA	0.86	0.92	0.62	0.92	0.21
$k-\epsilon$ + CA	0.85	0.93	0.63	0.91	0.22
$k-\omega$ + CA	0.85	0.88	0.57	0.92	0.17
$k-kl$ + KC	0.85	0.94	0.63	0.90	0.13

a wall function for the kl equation to represent the effect of the free surface and the bottom, and this may cause the closure to break down for strongly layered flows. There are also multiple choices of wall functions and no single choice can be applied universally.

[51] The reasonable performance of $k-kl$ may imply that our domain to great extent resembles a wall-bounded open channel flow with weak wind effects. In the present work, observations do not show a strong wind effect in the inner estuary [*Giddings et al.*, 2011] and so wind effects are not accounted for, but it is possible that the daily variability in the observed bottom salinity that is not captured by the model is caused by offshore wind-driven mixing of the plume.

5. Temporal Characteristics of the Turbulence

[52] While the field program [*Giddings et al.*, 2011] was limited to the vicinity of the tip of Jetty Island, we take advantage of the spatial coverage of our model results to analyze the spatiotemporal variability of turbulence and mixing along the entire longitudinal extent of the salinity front. We compare the results at two locations, namely, (1) mooring site M3b and (2) location R09. Mooring site M3b was used for validation in section 3 and is located near the downstream end of the salt wedge during periods of strong stratification (roughly 6 km from point E in Figure 2), Location R09 is located roughly in the middle of the salt wedge (9 km from point E along the E–E' transect in Figure 2) and this location does not have companion measurements from the observational program. It provides a more complete time history of the salt wedge evolution and in this section we focus on the temporal variability of the turbulence.

5.1. TKE, Shear Production, and Buoyant Destruction

[53] Predicted time series of the vertical structure of salinity, TKE, shear production P and buoyant destruction $-B$ are shown in Figure 12 for mooring site M3b and location R09 for one tidal cycle. The salinity time series (Figures 12a and 12b) indicate that the water column

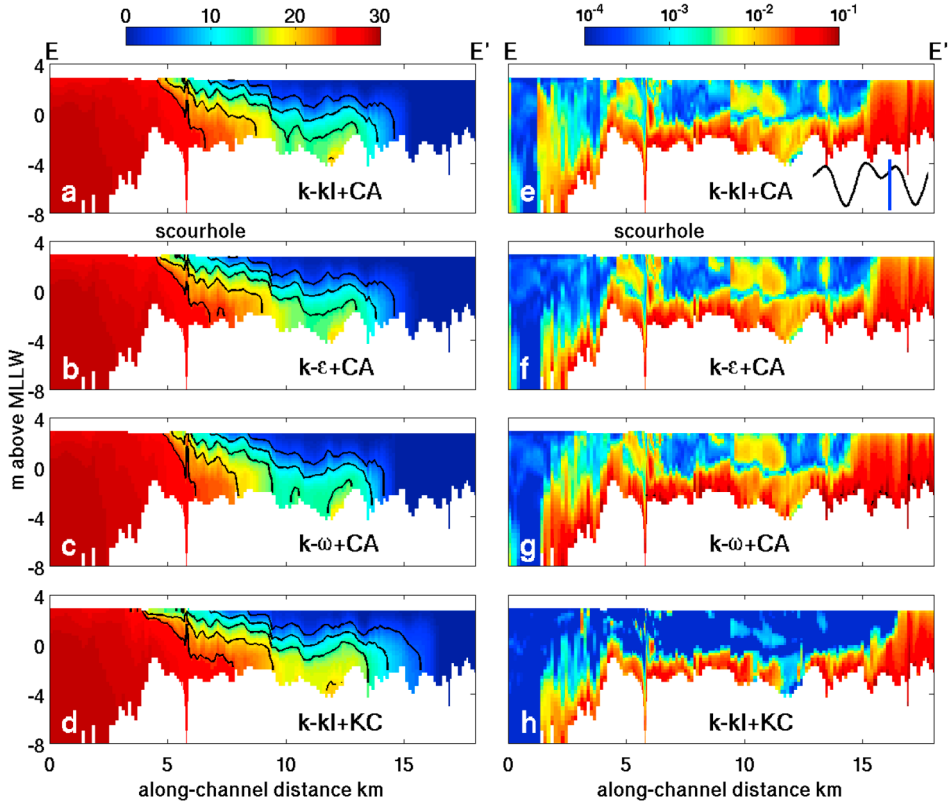

Figure 11. (a–d) Salinity (psu) and (e–h) TKE ($m^2\ s^{-2}$) distribution in the salt wedge developed during the weak flood of spring tide (year day 193) along transect E–E' from different closures. The tidal stage is shown in the bottom right corner of Figure 11e. Contour lines are for every 5 psu from 5 to 25 psu.

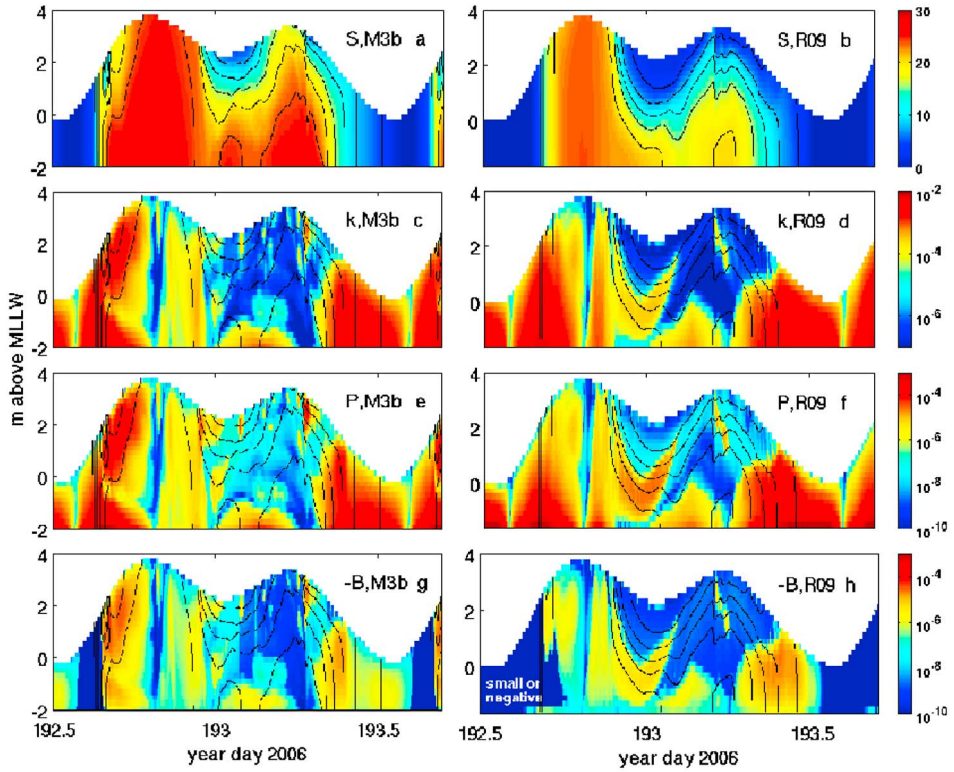

Figure 12. Time series of predicted (a and b) salinity (psu), (c and d) TKE ($m^2\ s^{-2}$), (e and f) shear production ($m^2\ s^{-3}$), and (g and h) buoyant destruction ($m^2\ s^{-3}$) in the TKE equation at two locations: (left) mooring site M3b and (right) an upstream location R09 (see locations in Figure 2). Salinity contours are plotted every 4 psu in Figures 12a and 12b. Results are from the $k - kl$ closure with the CA stability functions.

becomes mixed during strong ebb and then fresh near low low water at both locations. During the strong flood, the saline water reaches location R09 slightly later because it is further upstream and the water column is well mixed. However, at mooring site M3b, the near-surface salinity is disturbed by fresh water from the bypass late in the strong flood (around year day 192.7). Later on, the sharp salinity front of the salt wedge with buoyant water near the free surface traverses location R09 during the middle of weak ebb although it does not reach mooring site M3b until the end of weak ebb.

[54] Strong stratification persists throughout the weak flood at both locations as the isohalines are raised higher in the water column. Rapid decay of stratification and growth of turbulence begins to occur approximately at the same time at both locations.

[55] Strong ebbing flow advects the salinity front to the river mouth, creating straining which acts to stratify the water column and competes with the bottom-generated turbulence and mixing.

[56] The predicted TKE (Figures 12c and 12d) and the shear production P (Figures 12e and 12f) share similar features, since shear production is a good indicator of TKE. However, during the unstratified (fresh or well-mixed) period the near-surface layer has a very low shear production rate (as velocity gradient diminishes) while the TKE maintains a baseline value. The strongest turbulence is predicted during the strong tide as expected.

[57] During the weak ebb, turbulence first grows over the extent of the water column until it is suppressed by the strong stratification of the salt wedge. This feature is more prominent at location R09 than mooring site M3b.

[58] When strongly stratified, the results at location R09 (Figures 12d and 12f) depict a layer of strong turbulence at an intermediate depth which follows the density interface where strong shear exists.

[59] This feature is not present at mooring site M3b because the salt wedge has not propagated far enough downstream until the subsequent weak flood. During the weak flood, the middepth turbulent layer vanishes and a near-bottom mixed layer forms instead. This bottom layer is present at both location R09 and mooring site M3b and it grows with the barotropic tidal currents but never expands to the upper water column. At this time, the velocity profile (profile f in Figure 7) has a maximum at middepth due to the combined effects of barotropic and baroclinic pressure, and thus above that depth the strain continues to stabilize the flow while below it the strain destabilizes the flow and leads to production of TKE in the lower layer. During the subsequent strong ebb, strong turbulence grows and eventually expands over the entire water column. One important finding is that the TKE initially grows in the middle of the water column along the density interface at mooring site M3b, while TKE is bottom-generated at location R09, which demonstrates the spatial inhomogeneity along the salt wedge. These qualitative characteristics of the TKE dynamics pre-

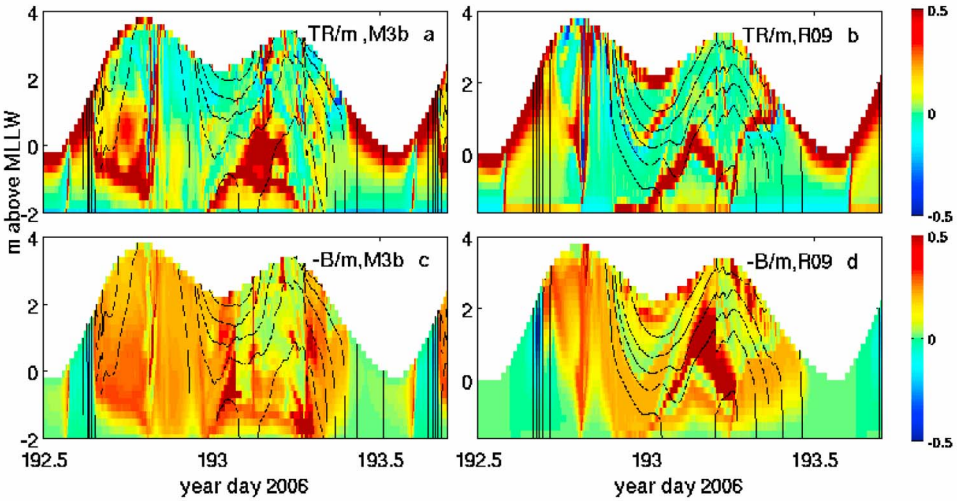

Figure 13. (a and b) Transport and (c and d) buoyant destruction of TKE normalized by the total available mechanical energy m at mooring site M3b (Figures 13a and 13c) and location R09 (Figures 13b and 13d). Salinity contours are plotted for every 4 psu in Figures 13a and 13b.

dicted by the model agree with what is shown by our mooring observations [*Giddings et al.*, 2011] and earlier work by *Nepf and Geyer* [1996]. Nepf and Geyer discovered similar mixing patterns in which strong mixing occurs along the middepth shear layer during the weak ebb and the bottom mixed layer during weak flood in the Hudson River estuary during strongly stratified periods.

[60] Buoyant production/destruction B (defined in equation (8) and shown in Figures 12g and 12h) represents the TKE that is extracted from the turbulence and converted into mixing a stable density gradient when $B < 0$. In this text, $-B$ is used to indicate the intensity of mixing achieved by turbulence, and depends on both the strength of the turbulence (through κ_t) and the presence of stratification (through N^2). Therefore, it is related to but not equivalent to TKE or P.

[61] Around low low water when the flow is unstratified, $|B|$ is small and negative most of the time due to the presence of very weak stratification, but is positive at times due to the overturning strain of flood tide.

[62] At both mooring site M3b and location R09, one of the most important mixing periods during a tidal cycle is the strong ebb when the stratification decays rapidly. However, at mooring site M3b, another strong mixing period occurs late in the strong flood at the confluence, while at location R09, a second strong mixing event takes place within the middepth shear layer during the weak ebb. The mixing in the bottom mixed layer that develops during the weak flood is small in comparison to the mixing mentioned above.

5.2. TKE Balance and the Role of Transport

[63] To analyze the dominant terms in the TKE equation, we write the TKE equation (6) as

$$P + B - \epsilon + TR - \frac{\partial k}{\partial t} = 0, \tag{17}$$

where TR represents transport of TKE including both diffusive and advective effects. Positive TR indicates that transport acts to increase TKE while negative TR indicates a sink of TKE. The unsteadiness of TKE, $\frac{\partial k}{\partial t}$, is always two orders of magnitude smaller than the dominant terms in the equation, implying that the other terms are roughly in equilibrium throughout the simulation period. We therefore neglect the unsteadiness for simplicity in what follows. Following *Ivey and Imberger* [1991], we define $m = \epsilon - B$ or $P + TR$ as the total amount of mechanical energy available for dissipation per unit volume per second. The computed values used in solving the TKE equation in our model are used to compute the terms in equation (17), and because the boundary fluxes for the TKE are zero, no special treatment at the top and bottom cells is required.

[64] The relative importance of the transport as a source and buoyant production as a sink are illustrated in Figure 13 with normalized quantities TR/m and $-B/m$. The normalized transport (Figures 13a and 13b) shows that for most of the time, transport is small and local shear production is the main source except for a few thin layers due to three primary mechanisms. First, similar to open channel flow, during the well-mixed strong tide, the shear production near the free surface approaches zero while the dissipation rate approaches some small finite value [see *Nakayama and Yokojima*, 2003]. In this region the imbalance between dissipation and production is accounted for by vertical diffusion, which leads to a thin near-surface layer of relatively important transport TR.

[65] Second, transport is important in the outer boundary of the bottom mixed layer that develops during the weak flood. This region represents the transition between the boundary layer where shear production and dissipation are in balance and the pycnocline where dissipation is in balance with both shear and buoyant production. The positive TR here represents upward transport of TKE from the boundary layer that is lost upon encountering the stratification. These two types of regions in which transport plays an important role are general features present at both mooring site M3b and location R09. At mooring site M3b, transport of TKE appears to be important at the interfacial layer between the two converging water masses late in the strong flood (around day 192.7).

[66] In summary, the predictions show that transport can be the main source of TKE in three types of thin regions: a near-surface layer, the outer boundary of the bottom-mixed layer and the interface of the two water masses at the confluence. Outside of these layers, the predominant source in most of the domain is shear production.

[67] The normalized buoyant destruction $-B/m$ is equal to the flux Richardson number $R_f = -B/(\epsilon - B)$ [*Ivey and Imberger*, 1991], which describes the portion of energy that is lost to mixing and represents the efficiency of mixing. Various observations [*Ivey and Imberger*, 1991; *Stacey et al.*, 1999a] found that the highest mixing efficiency, i.e., the maximum value of R_f, is roughly 0.15 to 0.25 and occurs under weakly stratified conditions. Figures 13c and 13d illustrate the predicted $R_f = -B/m$ at mooring site M3b and location R09, respectively. It should be noted that there are unphysically large R_f values predicted within strongly stratified regions where turbulence is rather weak (e.g., at middepth of day 193.2 at location R09 where the eddy viscosity is on the order of 10^{-9} m^2 s^{-1}). These values result from the minimum values set in the turbulence closures and have no physical meaning, since physically R_f should decay to zero under such conditions [*Ivey and Imberger*, 1991]. Outside of the regions of unphysically high R_f, R_f is around 0.2 when the flow is weakly stratified, and decreases to zero within the bottom mixed layer or during the well-mixed strong tide. This indicates that the predicted mixing efficiency is quite optimal for a large portion of the time, although the value is slightly greater than the maximum efficiency previously found in stratified systems from observations [*Stacey et al.*, 1999a] and models [*MacCready et al.*, 2009].

6. Longitudinal Dynamics of the Salt Wedge

6.1. Longitudinal Dynamics of Salinity and Vertical Mixing

[68] In what follows, we examine the spatial variability of turbulent mixing and the potential energy anomaly to analyze their roles in the development of the salt wedge at different phases of a tidal cycle. The potential energy anomaly Ψ is defined as $\Psi = \frac{g}{D}\int_{z_b}^{z_t}(\overline{\rho} - \rho)z dz$, where z_t and z_b are the elevation of the top and bottom of the water column, respectively, $\overline{()} = \frac{1}{D}\int_{z_b}^{z_t}() dz$ is the depth-averaging operator, and $D = z_t - z_b$ is the local depth. The potential energy anomaly is an approximation of the amount of energy needed per unit volume to convert a stratified water column to its well-mixed state, and is often used to represent the strength of the vertical stratification [*Simpson and Hunter*, 1974; *Nunes Vaz et al.*, 1989]. For a homogeneous vertical density profile, $\Psi = 0$, while $\Psi > 0$ in the presence of stable stratification. To include the effect of varying depth of a water column, we use the product $D\Psi$ to represent the energy needed per unit area to fully mix a water column.

[69] The salt transport equation (equation (4)) can be transformed to the equation for density transport to yield

$$\frac{\partial \rho}{\partial t} + \nabla \cdot (\mathbf{U}\rho) = \kappa_H \nabla_H^2 \rho + \frac{\partial}{\partial z}\left[(\kappa_t + \kappa)\frac{\partial \rho}{\partial z}\right]. \tag{18}$$

[70] For illustration purposes, we derive the equation for $D\Psi$ in a simplified case in which the free surface gradient and bottom slope are negligible. First, the equation for the depth-averaged density $\overline{\rho}$ can be obtained by integrating equation (18) with respect to z from z_b to z_t and dividing by the depth D to give

$$\frac{\partial \overline{\rho}}{\partial t} + \nabla_H \cdot \left(\overline{\mathbf{U}_\mathbf{H}}\overline{\rho} + \overline{\widetilde{\mathbf{U}}_\mathbf{H}\widetilde{\rho}}\right) = \kappa_H \nabla_H^2 \overline{\rho}, \tag{19}$$

where $\widetilde{()}$ implies deviation from the depth-averaged value, i.e., for ρ, $\rho = \overline{\rho} + \widetilde{\rho}$, and $\mathbf{U}_H$ is the horizontal velocity vector. We note that the vertical advection or diffusion do not affect $\overline{\rho}$ explicitly. Subtracting equation (18) from equation (19), multiplying by gz and integrating with respect to z over the water column yields the relation for Ψ,

$$\begin{aligned}\frac{\partial}{\partial t}(D\Psi) = &\underbrace{-\rho_0 \int_{z_b}^{z_t} B dz}_{\text{Vertical Mixing}} + \underbrace{\int_{z_b}^{z_t}(\rho - \overline{\rho})gw dz - \int_{z_b}^{z_t}\overline{\rho}gw dz + (w\overline{\rho}gz)|_{z=z_t}}_{\text{Conversion}} \\ &\underbrace{-\nabla_H \cdot (\overline{\mathbf{U}_\mathbf{H}} D\Psi)}_{\text{Translation}} + \underbrace{\nabla_H \cdot \left(\overline{\rho}\int_{z_b}^{z_t}\widetilde{\mathbf{U}}_\mathbf{H} g z dz\right)}_{\text{Straining}} + \underbrace{\kappa_H \nabla_H^2 (D\Psi)}_{\text{Diffusion}}.\end{aligned} \tag{20}$$

[71] This equation shows that the change in the potential energy anomaly results from local mixing, conversion from kinetic energy through vertical motion, horizontal advection (translation and straining) and diffusion. The conversion terms associated with the depth-averaged density field and anomaly are written separately for easier interpretation of the physics. When the free surface gradient and bottom slope are significant, the mathematical form of the conversion and transport terms are more complicated, while the vertical mixing term remains unchanged. Therefore, we will use equation (19) to compare the time rate of change of the potential energy anomaly to vertical mixing. Rather than compute the other terms, we will attribute their combined sum to potential imbalances between the time rate of change of the potential energy anomaly and the vertical mixing.

[72] The salinity contours, profiles of buoyant destruction (to indicate mixing, since $B < 0$), depth-averaged salinity, and $D\Psi$ (to indicate stratification) along transect E–E' are depicted in Figure 14. At LLW the salinity gradient is outside the mouth of the estuary and forms a river plume (Figure 14a). The strong flood advects the salinity front upstream to x = 15 km from location E, and by the end of the flood, the highest depth-averaged horizontal salinity gradient is situated at roughly 12 km near the upstream end of the estuary (Figure 14b). Relatively strong mixing occurs around 6 km at the confluence of the bypass flow, as a result of stronger turbulence as well as continuous input of buoyant flow from the bypass. Early in the subsequent weak ebb, the combined effects of straining and baroclinic pressure gradients lead to weak vertical stratification along the estuary that is quickly mixed by the turbulence throughout the depth in most regions. However, stratification continues to strengthen in the upstream reach where the horizontal salinity gradient is high (Figure 14c). The stable salt wedge is well established later in the weak ebb (Figure 14d), and the middepth shear layer with strong mixing that we observed earlier in the temporal dynamics (Figure 12) appears as a prominent feature along the entire horizontal extent of the salt wedge.

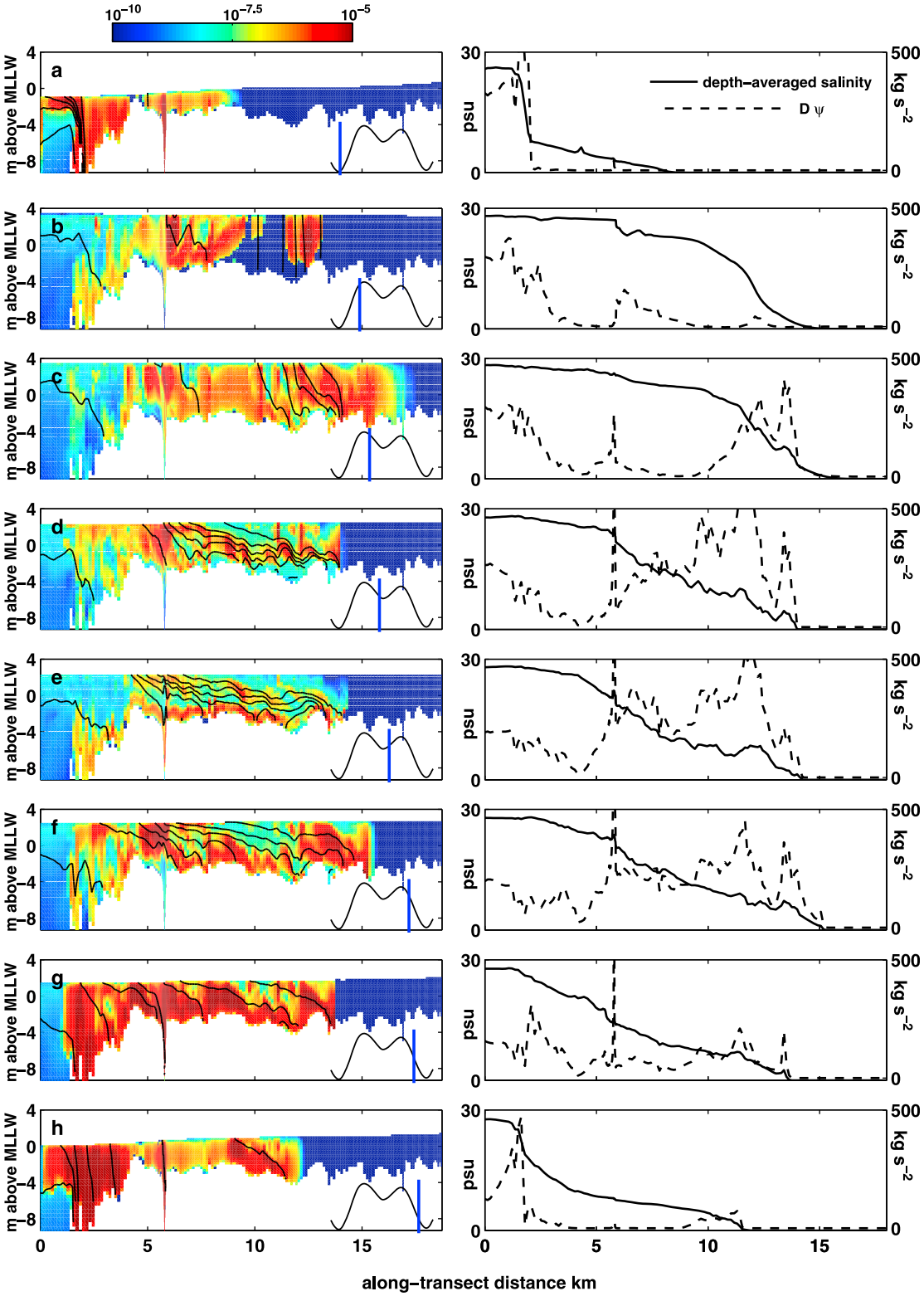

Figure 14. Longitudinal profiles of (left) buoyant destruction rate $-B$ (m^2 s^{-3}) and salinity contours (psu) and (right) depth-averaged salinity and $D\Psi$ at different stages of one tidal cycle along transect E–E' : (a) beginning of strong flood, (b) end of strong flood, (c) weak ebb, (d) end of weak ebb, (e) weak flood, and (f–h) strong ebb. Salinity contours are for every 4 psu, and tidal stages are shown in the bottom right corners of the plots in Figure 14 (left) and in Figure 15a.

[73] After the flow reverses to weak flood, stratification persists while the bottom-mixed layer grows along the salt wedge (Figure 14e), and this leads to a slight reduction in the overall stratification. Throughout the course of the weak ebb and flood, although the upstream location of the salinity front varies only by 1 km, the salt wedge expands as the downstream end is displaced by 5 km due to horizontal dispersion induced by gravitational circulation (Figure 14e). Gravitational circulation and ebb-induced straining reduce the depth-averaged horizontal salinity gradient of the salt wedge which had been compressed by the previous strong flood tide, resulting in regions of strong horizontal salinity gradients at its upstream and downstream ends. Then, at the early stage of the strong ebb (Figure 14f), the mixing pattern is quite inhomogeneous along the salt wedge: near the ends of the salt wedge mixing occurs throughout the depth in a similar manner to that early in the weak ebb (Figure 14c) because of the strain-induced stratification, while along the middle stretch of the salt wedge mixing is limited to the bottom because of the absence of significant horizontal density gradients. As the tidal flow accelerates, the mixed layer expands throughout the water column and over the entire extent of the salinity front (Figure 14g). Toward the end of the strong ebb, the salinity front is advected outside the estuary and intense mixing occurs within the river plume formed offshore (Figure 14h). Throughout the tidal cycle, there is persistent intensified mixing at the steep scour hole and sill 6 km upstream of location E due to the abrupt bathymetry.

[74] We integrate the potential energy anomaly and the buoyant destruction along transect E–E' to illustrate the overall temporal variability in the stratification and mixing over a tidal cycle. The integrated potential energy anomaly and integrated buoyant destruction are defined as

$$\Psi_{int} = \int_{x_1}^{x_2} D(x')\Psi(x')dx', \tag{21}$$

$$BD_{int} = \rho_0 \int_{x_1}^{x_2} \int_{z_b}^{z_t} -B(x', z)dx'dz, \tag{22}$$

where x' is the distance along transect E–E', and we exclude all $B > 0$ in the calculation (i.e., B is set to 0 when $B > 0$). Although calculated along a vertical transect, these quantities can represent the estuarine-scale dynamics very well because the inner estuary is long and does not vary significantly in the lateral direction. Figure 15 shows the results of Ψ_{int} and BD_{int} which are integrated over transect E–E' and Ψ'_{int} and BD'_{int} which are integrated along the inner part of the transect for the shallow estuary (excluding the first 4 km of the transect). The anomalies increase rapidly during the weak ebb as the stratification develops, retain their magnitudes during the weak flood while fluctuating slightly, and reach their maximum values near the beginning of the strong ebb (Figure 15b). Strong decreases in the anomalies occur later in the strong ebb, during which time the decay rates result from large mixing rates (Figure 15c) as well as downstream advection of the salinity front. These processes manifest themselves as two peaks in the value of BD_{int} during strong ebb, as shown in Figure 15c. The first peak is due to mixing along the estuary (see Figure 14g), while the second peak occurs when the salinity front is advected downstream and into the river mouth (see Figure 14h). Because it does not include the river mouth, BD'_{int} only shows the first peak which results from mixing in the estuary.

[75] To demonstrate the importance of local mixing, we compare BD'_{int} to the time rate of change of Ψ'_{int} for the inner estuary (Figure 15d), the relationship between the two quantities described by equation (19). The results show that during the weak tide the stratification exhibits weak oscillations and progressively becomes stronger (i.e., $(-\partial\Psi'_{int}/\partial t) < 0$). Five particular events associated with these oscillations are indicated in Figure 15d. In events 1 and 5, stratification strengthens due to the combined effects of ebb-induced strain and gravitational circulation which act to advect fresh water over salt water, in what is commonly referred to as SIPS [*Simpson et al.*, 1990]. In event 3, which occurs at the beginning of the weak flood, the straining in the upper water column due to gravitational circulation continues to stabilize the water column despite a reversal in the barotropic current direction (refer to the velocity profile at mooring site M3b in profiles e and f in Figure 7). The stratification increases considerably at the downstream end of the salt wedge as the flood advects deep saline water up into the estuary which compresses the density gradient there (Figures 14d and 14e). Events 2 and 4 correspond to two short periods of weak reduction in the stratification ($(-\partial\Psi'_{int}/\partial t) > 0$). Event 2 occurs at the end of the weak ebb when the flow and straining become weak and cease to further intensify the stratification. Local mixing dominates during this process as indicated by the approximate balance between $-\partial\Psi'_{int}/\partial t$ and BD'_{int}. Event 4 occurs during peak flow of the weak flood and the decay rate exceeds BD'_{int} indicating that destabilizing straining may be significant. A similar process occurs at peak flow during the strong flood around day 192.6. Overall, BD'_{int} is small compared to the magnitude of $-\partial\Psi'_{int}/\partial t$ during the weak tide, and thus local mixing does not significantly influence the stratification during this period. However, during strong ebb mixing events, local mixing is substantial and accounts for roughly half of the decay rate of Ψ'_{int}.

6.2. Response of the Stratification to Changes in the Buoyant Destruction

[76] Because stratification, once established, will suppress turbulent mixing and further intensify stratification, the nonlinear interaction between stratification and turbulent mixing is an essential element of the estuarine salt dynamics. We investigate how stratification responds to changing conditions in the turbulence by adjusting how the stratification affects the turbulence in the model. A coefficient γ is added to the buoyant production/destruction terms in the original TKE and length scale equations, such that equations (6) and (7) become

$$\frac{\partial k}{\partial t} + \nabla \cdot (\mathbf{u}k) = \frac{\partial}{\partial z}\left(\frac{\nu_t}{\sigma_k}\frac{\partial k}{\partial z}\right) + P + \gamma B - \epsilon, \tag{23}$$

$$\frac{\partial \psi}{\partial t} + \nabla \cdot (\mathbf{u}\psi) = \frac{\partial}{\partial z}\left(\frac{\nu_t}{\sigma_\psi}\frac{\partial \psi}{\partial z}\right) + \frac{\psi}{k}(c_1 P + \gamma c_3 B - c_2 \epsilon F_{wall}). \tag{24}$$

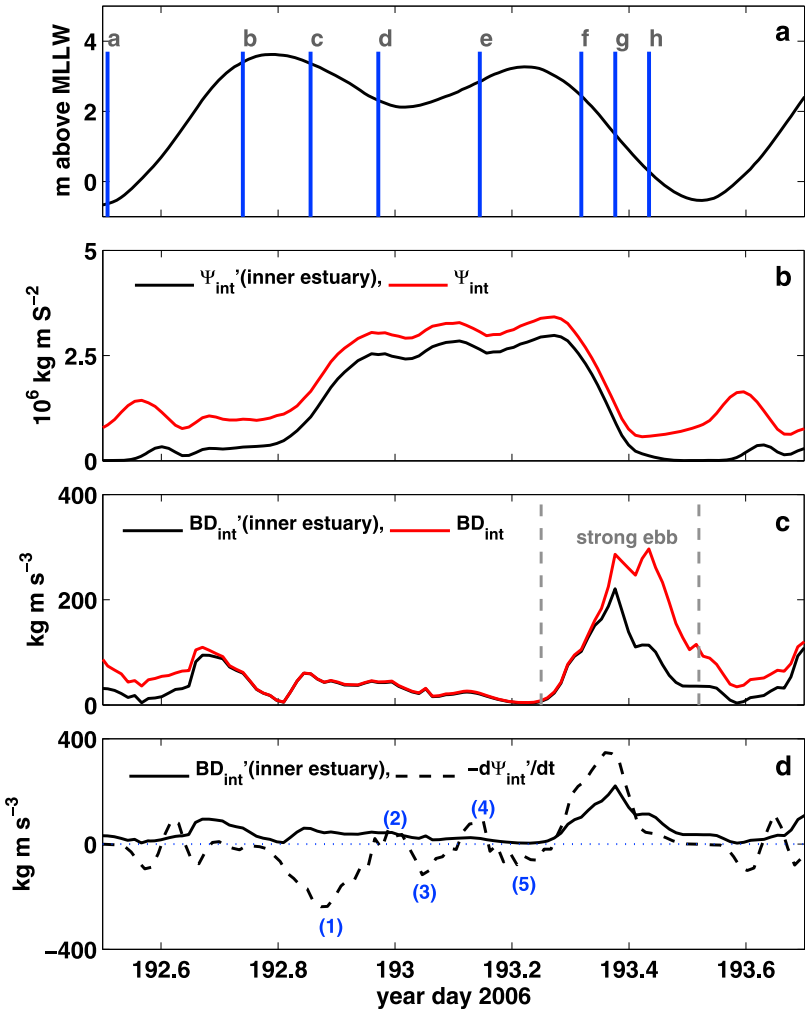

Figure 15. (a) Tide and the time stamps for profiles a–h in Figure 14. (b–d) Time series of the integrated potential energy anomaly and buoyant destruction along transect *E*–*E*′ over one tidal cycle.

[77] Setting $\gamma = 1$ retrieves the original equations, while a larger value of γ leads to stronger suppression of turbulence by stratification. Numerical simulations were performed for hypothetical conditions with $\gamma = 2$, 0.5, for a moderate effect, and $\gamma = 10$, 0.1 to demonstrate more extreme cases. The simulations with different values of γ were all initialized with the same initial conditions during LLW around day 192.5 which were obtained from the model with $\gamma = 1$.

[78] Figure 16 depicts longitudinal profiles of buoyant destruction, depth-averaged salinity, and $D\Psi$ at the end of the weak ebb using different values of γ. The results show that larger values of γ (Figures 16a and 16b) lead to sharper vertical density gradients and a prolonged horizontal extent of the salt wedge. The mixing along the middepth interfacial layer is also significantly reduced. Smaller γ values yield considerably weaker stratification as depicted in Figures 16d and 16e, which show much smaller values of the potential energy anomaly. In the case of $\gamma = 0.1$ (Figure 16e), the isopycnals are almost uniformly spaced with no clear interfacial layer as a result of very weak nonlinear interaction between stratification and turbulence.

[79] Time series of the integrated potential energy anomaly Ψ'_{int} and buoyant destruction BD'_{int} for the inner estuary are presented in Figure 17. Figure 17b shows the increasing intensity of stratification during the weak tide with increasing γ. For $\gamma = 2$ and 10, stratification persists during the strong ebb and the decrease in Ψ'_{int} is mainly caused by advection of the salinity front offshore. The relationship between the maximum value of Ψ'_{int} and the value of γ is illustrated by the inset in Figure 17b. For an intermediate range of $\gamma = 0.5$–2, Ψ'_{int} is highly sensitive to changes in γ, while the sensitivity decreases rapidly for $\gamma =$ 0.1 and 10 (note the log scale for γ). Our interpretation is that the actual conditions in the estuary result from a delicate balance between mixing and intermediate levels of stratification, while the nonlinear interaction between turbulence and stratification becomes less dynamic under more extreme conditions. Under these extreme conditions (strong or no stratification), the salinity dynamics is controlled by other factors, such as the magnitude and straining of the tidal currents, river inflow, and mixing at the river mouth during LLW. Figure 17c shows that the integrated mixing rates

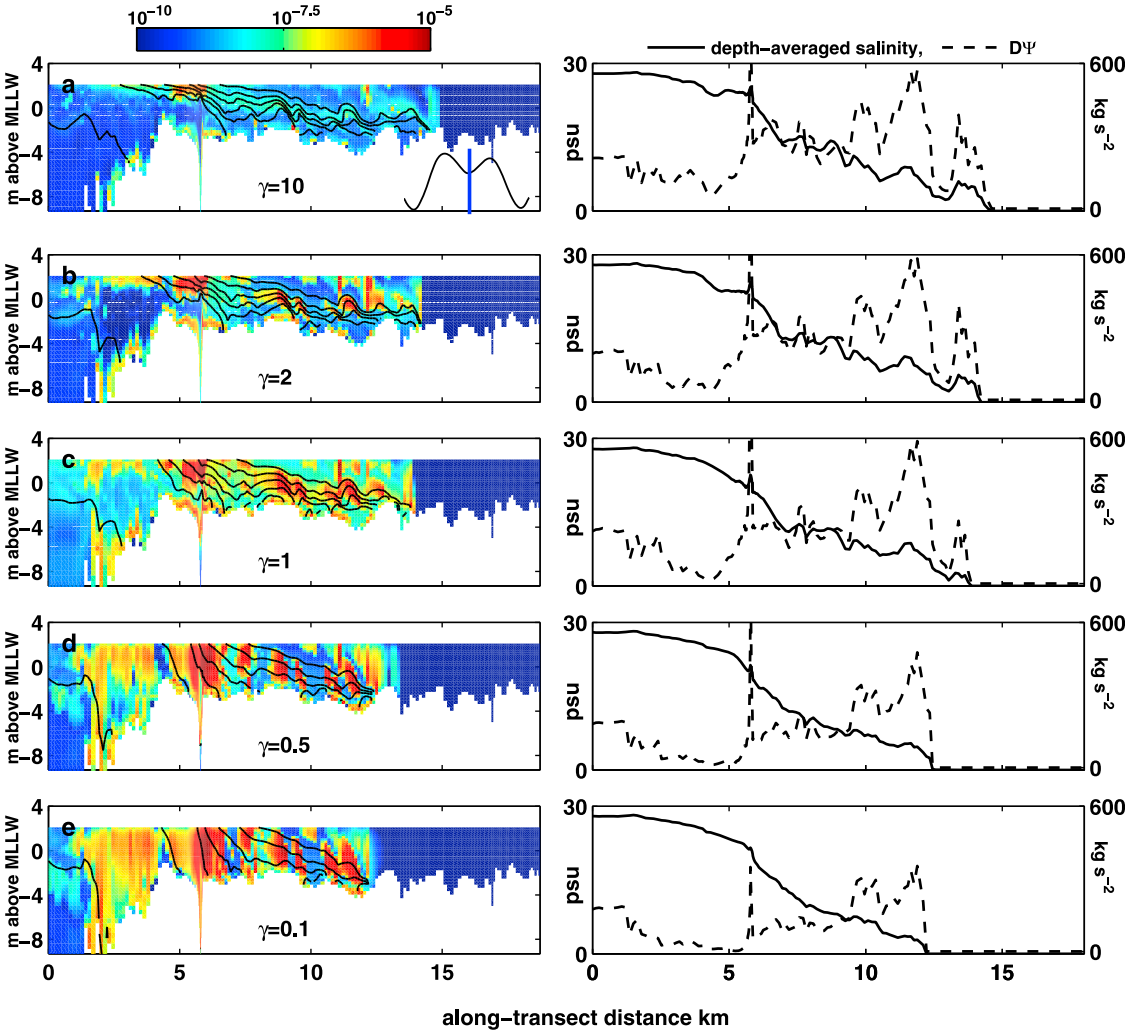

Figure 16. Longitudinal profile of (left) buoyant destruction $-B$ ($m^2\ s^{-3}$) and (right) depth-averaged salinity and $D\Psi$ at the end of weak ebb along transect E–E' from simulations with (a) $\gamma = 10$, (b) $\gamma = 2$, (c) $\gamma = 1$, (d) $\gamma = 0.5$, and (e) $\gamma = 0.1$. Salinity contours are plotted over intervals of 4 psu in Figure 16 (left). The tidal stage is shown in Figure 16a.

generally increase and the peak mixing rates occur earlier with decreasing values of γ in the inner estuary. However, BD'_{int} does not change significantly when γ is reduced from 0.5 to 0.1. For these two cases, local mixing is so strong that it becomes the dominant term in the decay of stratification, i.e., $BD'_{int} \approx -\partial\Psi'_{int}/\partial t$ (see the relation in equation (19)). It is thus limited by the available potential energy anomaly, while for other cases, local mixing is competing with other effects, such as advection.

[80] Figure 17d depicts the integrated mixing rates along the entire transect E–E'. The mixing that occurs near the river mouth (the difference between Figures 17c and 17d) increases more considerably with decreasing γ than that in the inner estuary. The two peaks in the mixing during the strong ebb (described earlier) that are associated with mixing in the inner estuary and offshore from the river mouth persist for $\gamma = 0.1$ and 0.5, yet are absent for $\gamma = 2$ and 10. The first peak is absent for these cases because the ebbing currents do not destratify the water column in the inner estuary, but rather continuously mix at a lower rate over the strong ebb due to overdamping of the TKE.

7. Conclusions

[81] A high-resolution numerical model has been employed to study the intratidal variability of stratification and turbulent mixing in a shallow macrotidal estuary in which a stable salt wedge develops during the weak tide and decays significantly during the strong tide every tidal day. The unresolved vertical mixing is parameterized with the GLS closure scheme which shows no appreciable difference between different turbulent closure schemes ($k - kl$, $k - \epsilon$, $k - \omega$) in this energetic system. However, the difference between the stability functions is more pronounced and shows that the KC stability functions fail to predict fresh water at low tide. In general, due to a lower critical Richardson number required for mixing with the KC stability functions, vertical gradients are slightly stronger due

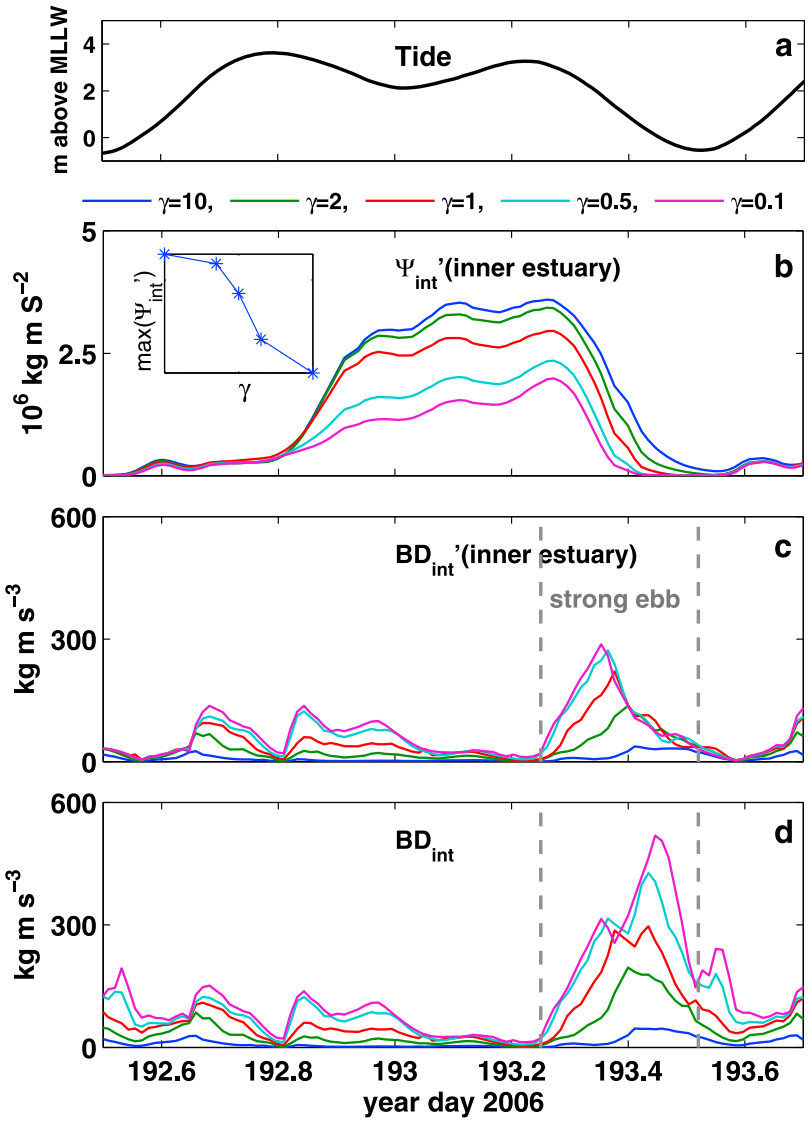

Figure 17. (a) The tidal stage. Time series of the (b) integrated potential energy anomaly, (c) buoyant destruction in the inner estuary (excluding the first 4 km of transect *E–E′*), and (d) the integrated buoyant destruction along the entire transect *E–E′* during two tidal cycles from simulations with different γ values. The relation between the maximum value of Ψ'_{int} and γ is shown in the inset in Figure 17b.

to an underprediction of mixing, thereby enabling more gravitational circulation and salt intrusion into the estuary.

[82] The results from the $k - kl$ (MY2.5) closure scheme with the CA stability functions are robust and used for our analysis. Validation is performed via comparison to observed vertical structure of velocity and salinity, Richardson number, and Reynolds stress, all of which show good agreement with the observations.

[83] The model results show that at the beginning of weak ebb, the stably stratified salt wedge forms near the upstream end of the salinity front where the horizontal salinity gradient is high, and the extent of the salt wedge gradually propagates downstream toward the river mouth throughout the weak tide. The model shows that active mixing is mainly confined to middepth within the density interface during the stratified period of weak ebb, and this is consistent with the findings inferred from mooring observations [*Giddings et al.*, 2011]. During the weak flood, on the other hand, active mixing is confined to a bottom mixed layer. This bottom mixed layer is characterized by an upper boundary in which vertical transport of TKE is in balance with local dissipation. A similar mixing pattern during the weak tide was also discovered by *Nepf and Geyer* [1996] in the Hudson estuary.

[84] The model predicts two major mixing events that take place during the strong ebb. The first corresponds to strong mixing along the entire length of the salt wedge in the shallow inner estuary (upstream of the mouth) which contributes to a rapid decay of the salt wedge. The second event occurs within the river plume formed at the river mouth when the salinity front is advected into the deeper waters offshore. The integrated buoyant destruction shows that the energy lost to mixing during the strong ebb greatly exceeds that during other stages of the tidal cycle. Overall, the strong

mixing and advection that occur during the strong tide flush the estuary and effectively reset the stratification at the beginning of every tidal cycle in a similar manner to what was observed in San Francisco Bay by *Ralston and Stacey* [2005]. This process is essential to the insensitivity of the results to the different turbulence models which cannot manifest their differences over such short time scales.

[85] By changing the magnitude of the buoyant production term in the TKE and length scale equations via multiplication by a constant, γ, the influence of the stratification on the turbulence could be assessed. In general, mixing is enhanced and stratification is reduced with small values of γ (weaker buoyant production), since suppression of TKE due to stratification is reduced. For the more strongly mixed cases (small γ), the amount of mixing during the breakdown of stratification is limited by the available potential energy anomaly, as local mixing accounts for almost all of the temporal decay of the potential energy anomaly. For the more stratified cases (large γ), only one peak mixing event occurs during a tidal day because of the lack of mixing during the strong ebb in the inner estuary. The sensitivity of the mixing dynamics to changes in γ (the magnitude of the buoyancy) is strong for values of $\gamma \sim 1$, which implies that the real system exists in a regime in which the interaction between turbulence and stratification is highly nonlinear. From a modeling point of view, it is this sensitivity that makes it so difficult to develop a universal parameterization for the buoyant production.

Notation

U,V,W Cartesian components of the mean velocity vector, m s^{-1}.
U mean velocity vector, m s^{-1}.
U_i Reynolds averaged velocity vector in Einstein notation, m s^{-1}.
u'_i fluctuating part of the velocity vector in Einstein notation, m s^{-1}.
S mean salinity concentration, psu.
s' fluctuating part of the salinity concentration, psu.
x_i Cartesian spatial coordinates in Einstein notation, m.
t time, s.
P Reynolds averaged pressure, Pascal.
g gravity acceleration, m s^{-2}.
ρ_0 reference density, kg m^{-3}.
ρ' density variation normalized by ρ_0.
f Coriolis force coefficient, s^{-1}.
ν, κ molecular viscosity and diffusivity, m^2 s^{-1}.
ν_H, κ_H horizontal eddy viscosity and eddy diffusivity, m^2 s^{-1}.
ν_t, κ_t vertical eddy viscosity and eddy diffusivity, m^2 s^{-1}.
k turbulent kinetic energy (TKE), $k \equiv \langle u'_i u'_i \rangle/2$, m^2 s^{-2}.
l turbulent macroscale for mixing, m.
ψ generic parameter of GLS, $\psi = (C_\mu^0)^p k^m l^n$.
C_μ^0 an empirical coefficient for dissipation.
P shear production rate of TKE, m^2 s^{-3}.
B buoyant production rate of TKE, m^2 s^{-3}.
ϵ dissipation rate of TKE, m^2 s^{-3}.
σ_k Schmidt number for the diffusion of TKE.
σ_ϕ Schmidt number for the diffusion of ϕ.
F_{wall} wall function for the $k - kl$ (MY2.5) closure.
κ_{VK} von Karman's constant, $\kappa_{VK} = 0.41$.
c_1, c_2, c_3 empirical constants for the length scale equation.
D_b, D_s distance to the bottom and surface, respectively, m.
E_2, E_3 constants in F_{wall} for the $k - kl$ closure, $E_2 = 1.33$, $E_3 = 0.25$.
c constant for ν_t and κ_t, varying with stability functions.
Δz distance from the near-wall cell center to the top or bottom surface, m.

[86] **Acknowledgments.** The authors wish to acknowledge Robert Street for his invaluable advice on various aspects of the work and Mark Stacey, John Warner, W. Rockwell Geyer, and David Ralston for their useful comments and suggestions. We also thank members of the COHSTREX project for their help with the observations and with obtaining accurate bathymetry. This research was supported by ONR grant N00014-05-1-0177 (scientific officers were Thomas Drake, Terri Paluszkiewicz, and C. Linwood Vincent) and the Stanford Graduate Fellowship (Wells Family Fellow). Simulations were performed on the JVN and MJM clusters at the ARL Major Shared Resource Center as part of a DOD Challenge Allocation.

References

Allen, J., P. Somefield, and F. Gilbert (2007), Quantifying uncertainty in high-resolution coupled hydrodynamic-ecosystem models, *J. Mar. Syst.*, *64*, 3–14.

Blumberg, A. F., B. Galperin, and D. J. O'Connor (1992), Modeling vertical structure of open-channel flows, *J. Hydraul. Eng.*, *118*, 1119–1134.

Bowden, K. F. (1981), Turbulent mixing in estuaries, *Ocean Manage.*, *6*, 117–135.

Burchard, H., and O. Petersen (1999), Models of turbulence in the marine environment. A comparative study of two equation turbulence models, *J. Mar. Syst.*, *21*, 29–53.

Canuto, V. M., A. Howard, Y. Cheng, and M. S. Dubovikov (2001), Ocean turbulence I: One-point closure model—Momentum and heat vertical diffusivities, *J. Phys. Oceanogr.*, *31*, 1413–1426.

Casulli, V., and E. Cattani (1994), Stability, accuracy and efficiency of a semi-implicit method for three-dimensional shallow water flow, *Comput. Math. Appl.*, *27*, 99–112.

Chen, C., H. Liu, and R. C. Beardsley (2003), An unstructured, finite-volume, three-dimensional, primitive equation ocean model: Application to coastal ocean and estuaries, *J. Atmos. Oceanic Technol.*, *20*, 159–186.

Chickadel, C. C., A. R. Horner-Devine, S. A. Talke, and A. T. Jessup (2009), Vertical boil propagation from a submerged estuarine sill, *Geophys. Res. Lett.*, *36*, L10601, doi:10.1029/2009GL037278.

Deleersnijder, E., J. M. Beckers, J. M. Campin, M. El Monhajir, and P. Luyten (1997), Some mathematical problems associated with the development and use of marine models, in *The Mathematics of Models for Climatology and Environment*, edited by J. I. Diaz, pp. 39–86, Springer, Berlin.

Fram, J. P., G. Gerbi, and W. R. Geyer (2003), Longitudinal and lateral salt gradients of the Snohomish River estuary: Summer research project at Friday Harbor Laboratories, *Eos Trans. AGU*, *84*(52), Ocean Sci. Meet. Suppl., Abstract OS42A-10.

Fringer, O., M. Gerritsen, and R. Street (2006), An unstructured-grid, finite-volume, nonhydrostatic, parallel coastal ocean simulator, *Ocean Modell.*, *14*, 139–173.

Galperin, B., L. H. Kantha, S. Hassid, and A. Rosati (1988), A quasi-equlibrium turbulent energy model for geophysical flows, *J. Atmos. Sci.*, *45*, 55–62.

Geyer, W. R., and D. M. Farmer (1989), Tide-induced variation of the dynamics of a salt wedge estuary, *J. Phys. Oceanogr.*, *19*, 1060–1072.

Giddings, S. N., D. A. Fong, and S. G. Monismith (2011), The role of straining and advection in the intratidal evolution of stratification, vertical mixing, and longitudinal dispersion of a shallow, macrotidal, salt-wedge estuary, *J. Geophys. Res.*, doi:10.1029/2010JC006482, in press.

Gross, E., J. Koseff, and S. Monismith (1999), Three-dimensional salinity simulations of south San Francisco Bay, *J. Hydraul. Eng.*, *125*, 1199–1209.

Ilicak, M., T. M. Özgökmen, H. Peters, H. Z. Baumert, and M. Iskandarani (2008), Performance of two-equation turbulence closures in three-

dimensional simulations of the Red Sea overflow, *Ocean Modell.*, *24*, 122–139.
Ivey, G. N., and J. Imberger (1991), On the nature of turbulence in a stratified fluid. Part I: The energetices of mixing, *J. Phys. Oceanogr.*, *21*, 650–658.
Jay, D. A., and J. D. Smith (1990a), Residual circulation in shallow estuaries. II: Weakly stratified and partially stratified, narrow estuaries, *J. Geophys. Res.*, *95*, 733–748.
Jay, D. A., and J. D. Smith (1990b), Circulation, density structure and neap-spring transitions in the Columbia River estuary, *Prog. Oceanogr.*, *25*, 81–112.
Jones, W. P. (1994), Turbulence modelling and numerical solution methods for variable density and combusting flows, in *Turbulent Reacting Flows*, edited by P. A. Libby and F. A. Williams, pp. 308–369, Academic, London.
Kantha, L. H., and C. A. Clayson (1994), An improved mixed layer model for geophysical applications, *J. Geophys. Res.*, *99*, 25,235–25,266.
Li, M., L. Zhong, and W. C. Boicourt (2005), Simulations of Chesapeake Bay estuary: Sensitivity to turbulence mixing parameterizations and comparison with observations, *J. Geophys. Res.*, *110*, C12004, doi:10.1029/2004JC002585.
Liu, Y., P. MacCready, B. M. Hickey, E. P. Dever, P. M. Kosro, and N. S. Banas (2009), Evaluation of a coastal ocean circulation model for the Columbia River plume in summer 2004, *J. Geophys. Res.*, *114*, C00B04, doi:10.1029/2008JC004929.
MacCready, P. (1999), Estuarine adjustment to changes in river flow and tidal mixing, *J. Phys. Oceanogr.*, *29*, 708–726.
MacCready, P., N. S. Banas, B. M. Hickey, E. P. Dever, and Y. Liu (2009), A model study of tide- and wind-induced mixing in the Columbia River estuary and plume, *Cont. Shelf Res.*, *29*, 278–291.
Mellor, G. L., and T. Yamada (1982), Development of a turbulence closure model for geophysical fluid problems, *Rev. Geophys.*, *20*(4), 851–875, doi:10.1029/RG020i004p00851.
Miles, J. (1961), On the stability of heterogeneous shear flows, *J. Fluid Mech.*, *10*, 496–508.
Monismith, S. G., and D. A. Fong (1996), A simple model of mixing in stratified tidal flows, *J. Geophys. Res.*, *101*(C12), 28,583–28,595, doi:10.1029/96JC02267.
Monismith, S. G., W. Kimmerer, J. R. Burau, and M. T. Stacey (2002), Structure and flow-induced variability of the subtidal salinity field in northern San Francisco Bay, *J. Phys. Oceanogr.*, *32*, 3003–3019.
Murphy, A. H. (1988), Skill score based on the mean square error and their relationship to the correlation coefficient, *Mon. Weather Rev.*, *116*, 2417–2424.
Nakayama, A., and S. Yokojima (2003), Modeling free-surface fluctuation effects for calculation of turbulent open-channel flows, *Environ. Fluid Mech.*, *3*, 1–21.
Nepf, H., and W. R. Geyer (1996), Intratidal variations in stratification and mixing in the Hudson estuary, *J. Geophys. Res.*, *101*, 12,079–12,086.
Nunes Vaz, R. A., G. W. Lennon, and J. R. de Silva Samarasinghe (1989), The negative role of turbulence in estuarine mass transport, *J. Geophys. Res.*, *28*, 361–377.
Peters, H. (1997), Observations of stratified turbulent mixing in an estuary: Neap-to-spring variations during high river flow, *Estuarine Coastal Shelf Sci.*, *45*, 69–88.
Plant, W. J., et al. (2009), Remotely sensed river surface features compared with modeling and in situ measurements, *J. Geophys. Res.*, *114*, C11002, doi:10.1029/2009JC005440.
Pope, S. B. (2000), *Turbulent Flows*, Cambridge Univ. Press, Cambridge, U. K.
Ralston, D. K., and M. T. Stacey (2005), Stratification and turbulence in subtidal channels through intertidal mudflats, *J. Geophys. Res.*, *110*, C08009, doi:10.1029/2004JC002650.
Ralston, D. K., W. R. Geyer, and J. A. Lerczak (2008), Subtidal salinity and velocity in the Hudson River estuary: Observations and modeling, *J. Phys. Oceanogr.*, *38*, 753–770.
Ralston, D. K., W. R. Geyer, and J. A. Lerczak (2010), Structure, variability, and salt flux in a strongly forced salt wedge estuary, *J. Geophys. Res.*, *115*, C06005, doi:10.1029/2009JC005806.
Rodi, W. (1987), Examples of calculation methods for flow and mixing in stratified fluids, *J. Fluid Mech.*, *92*, 5305–5328.
Shchepetkin, A., and J. C. McWilliams (2005), The Regional Oceanic Modeling System: A split-explicit, free-surface, topography-following-coordinate ocean model, *Ocean Modell.*, *9*, 347–404.
Simpson, J. H., and J. R. Hunter (1974), Fronts in the Irish Sea, *Nature*, *250*, 404–406.
Simpson, J. H., J. Brown, J. Matthews, and G. Allen (1990), Tidal straining, density currents, and stirring in the control of estuarine stratification, *Estuaries*, *13*, 125–132.
Simpson, J. H., H. Burchard, N. R. Fisher, and T. P. Rippeth (2002), The semi-diurnal cycle of dissipation in a ROFI: Model-measurement comparisons, *Cont. Shelf Res.*, *22*, 1615–1628.
Stacey, M. T., S. G. Monismith, and J. R. Burau (1999a), Observations of turbulence in a partially stratified estuary, *J. Phys. Oceanogr.*, *29*, 1950–1970.
Stacey, M. T., S. G. Monismith, and J. R. Burau (1999b), Measurements of Reynolds stress profiles in unstratified tidal flow, *J. Geophys. Res.*, *104*, 10,933–10,949.
Stips, A., H. Burchard, K. Bolding, and W. Eifler (2002), Modelling of convective turbulence with a two-equation $k - \epsilon$ turbulence closure scheme, *Ocean Dyn.*, *52*, 153–168.
Stow, C. A., J. Jolliff, D. J. McGillicuddy Jr., S. C. Doney, J. I. Allen, M. A. M. Friedrichs, K. A. Rose, and P. Wallhead (2009), Skill assessment for coupled biological/physical models of marine systems, *J. Mar. Syst.*, *76*, 4–15.
Umlauf, L., and H. Burchard (2003), A generic length-scale equation for geophysical turbulence models, *J. Mar. Res.*, *61*, 235–265.
Umlauf, L., and H. Burchard (2005), Second-order turbulence closure models for geophysical boundary layers. A review of recent work, *Cont. Shelf Res.*, *25*, 795–827.
Umlauf, L., H. Burchard, and K. Hutter (2003), Extending the $k - \omega$ turbulence model towards oceanic applications, *Ocean Modell.*, *5*, 195–218.
Wang, B., O. B. Fringer, S. N. Giddings, and D. A. Fong (2009), High-resolution simulations of a macrotidal estuary using suntans, *Ocean Modell.*, *26*, 60–85.
Warner, J. C., W. R. Geyer, and J. A. Lerczak (2005a), Numerical modeling of an estuary: A comprehensive skill assessment, *J. Geophys. Res.*, *110*, C05001, doi:10.1029/2004JC002691.
Warner, J. C., C. R. Sherwood, H. G. Arango, and R. P. Signell (2005b), Performance of four turbulence closure models implemented using a generic length scale method, *Ocean Modell.*, *8*, 81–113.
Wilcox, D. C. (1988), Reassessment of the scale-determining equation for advanced turbulence models, *AIAA J.*, *26*, 1299–1310.
Wilmott, C. (1981), On the validation of models, *Phys. Geogr.*, *2*, 184–194.
Yanagi, T., M. Shimizu, M. Nomura, and K. Furukawa (2003), Spring-neap tidal variations of residual flow in Tokyo Bay, Japan, *Cont. Shelf Res.*, *23*, 1087–1097.
Yang, Z., and T. Khangaonkar (2008), Modeling of salt intrusion, intertidal mixing, and circulation in a braided estuary, *J. Coastal Res.*, *52*, 171–180.

D. A. Fong, O. B. Fringer, S. N. Giddings, E. S. Gross, S. G. Monismith, and B. Wang, Environmental Fluid Mechanics Laboratory, Stanford University, Jerry Yang and Akiko Yamazaki Environmental and Energy Building, Rm. 126, Stanford, CA 94305, USA. (bingwang@stanford.edu)